

1 **Quasi-10-day wave activity in the southern high-latitude MLT**  
2 **region and its relation to the large-scale instability and**  
3 **gravity wave drag**

4

5 Wonseok Lee<sup>1</sup>, In-Sun Song<sup>1</sup>, Byeong-Gwon Song<sup>1</sup>, Yong Ha Kim<sup>2</sup>

6

7 <sup>1</sup>Department of Atmospheric Sciences, Yonsei University, Seoul 03722, South Korea

8 <sup>2</sup>Department of Astronomy and Space Science, Chungnam National University,

9 Daejeon 34134, South Korea

10

11 *Correspondence to:* In-Sun Song (songi@yonsei.ac.kr)

12

13 **Abstract.** Seasonal variation of westward-propagating quasi-10-day wave (Q10DW) in  
14 the mesosphere and lower thermosphere of the Southern Hemisphere (SH) high-latitude  
15 regions is investigated using meteor radar (MR) observations for the period of 2012–  
16 2016 and Specified Dynamics (SD) version of the Whole Atmosphere Community  
17 Climate Model (WACCM). The phase difference of meridional winds measured by two  
18 MRs located in Antarctica gives observational estimates of the amplitude and phase of  
19 Q10DW with zonal wavenumber 1 (W1). The amplitude of the observed Q10DW-W1 is  
20 large around equinoxes. In order to elucidate the variations of the observed Q10DW-W1  
21 and its possible amplification mechanism, we carry out two SD-WACCM experiments  
22 nudged towards the MERRA-2 reanalysis from the surface up to ~60 km (EXP60) and  
23 ~75 km (EXP75). Results of the EXP75 indicate that the observed Q10DW-W1 can be  
24 amplified around the barotropic/baroclinic instability regions in the middle mesosphere  
25 around 60°S–70°S. In the EXP60, it is also found that Q10DW-W1 is amplified around  
26 the instability regions, but the amplitude is too large compared with MR observations.  
27 The large-scale instability in the EXP60 in the SH summer mesosphere is stronger than  
28 that in the EXP75 and Microwave Limb Sounder observation. The larger instability in  
29 the EXP60 is related to the large meridional and vertical variations of polar mesospheric  
30 zonal winds in ~~association~~ with gravity wave parameterization (GWP). Given  
31 uncertainties inherent in GWP, these results can suggest that it is possible for models to  
32 spuriously generate traveling planetary waves such as Q10DW, especially in summer,  
33 due to the excessively strong large-scale instability in the SH high-latitude mesosphere.

Deleted: associated

## 35 1 Introduction

36 A series of Rossby normal modes (free oscillations) is the homogeneous solution  
37 of the governing equations on a sphere linearized with respect to the isothermal and  
38 quiescent reference atmosphere (e.g., Andrews et al., 1987; Forbes et al., 1995; Salby,  
39 1984). Traveling normal modes exhibit clear planetary-scale spatiotemporal oscillations  
40 throughout the whole atmosphere, and for sufficiently large amplitudes, these traveling  
41 planetary waves (PWs) can play an important role in the momentum and energy transfer  
42 to the mean flow (Salby, 1984). Three gravest traveling normal modes have been  
43 observed: Westward-propagating zonal-wavenumber-1 PWs with periods of  
44 approximately 5, 10, and 16 days. The classical wave theory based on the isothermal  
45 and quiescent atmosphere gives the theoretical periods of 5, 8.3, and 12.5 day, but the  
46 periods in the real atmosphere can be shifted to values close to 5, 10, and 16 days,  
47 respectively (Salby, 1981a, b), due to influences of the vertical and meridional variation  
48 of the mean horizontal winds and temperature.

49 Among the gravest modes, the quasi-5-day wave (Q5DW) and quasi-16-day  
50 wave (Q16DW) have extensively been studied through observations, modeling, and  
51 assimilation products: Ground-based observations (e.g., Day and Mitchell, 2010; He et  
52 al., 2020b; Mitra et al., 2022), satellite observations (e.g., Forbes and Zhang, 2017;  
53 Huang et al., 2022), reanalysis data (e.g., Huang et al., 2017), and simulations (e.g., Qin  
54 et al., 2021). Using meteor radars (MRs) located in the northern and southern polar  
55 regions, Day and Mitchell (2010) showed that PW activity is strong during winter and  
56 the seasonal variation of PW is similar in both polar regions. According to Qin et al.  
57 (2021) and Mitra et al. (2022), the barotropic and baroclinic instabilities are the possible

58 sources of Q5DW and Q16DW in that the waves can draw energy from the mean flow  
59 in the instability region. The disturbance of zonal-mean flow frequently occurs during  
60 the large-scale meteorological events such as sudden stratospheric warming (SSW). It  
61 has been reported that the amplitude of Q5DW or Q16DW increases during SSW events  
62 (Eswaraiah et al., 2016; Lee et al., 2021; Li et al., 2021; Ma et al., 2022). In addition,  
63 the amplified PWs can ~~interact with tidal waves~~ through the in-situ nonlinear  
64 interaction, resulting ionospheric disturbances during SSW (e.g., Goncharenko et al.,  
65 2020; Forbes et al., 2021; Liu et al., 2021; Qin et al., 2019).

**Deleted:** modulate the periods of tides

66 In contrast, the westward propagating quasi-10-day wave (Q10DW) with zonal  
67 wavenumber 1 (W1) has received little attention compared to the other gravest normal  
68 modes. Forbes and Zhang (2015) showed that Q10DW-W1 has a mean period of  $9.8 \pm$   
69  $0.4$  days using the temperature measurements from the Sounding of the Atmosphere  
70 using Broadband Emission Radiometry (SABER) instrument mounted on NASA's  
71 TIMED (Thermosphere Ionosphere Mesosphere Energetics Dynamics) satellite in  
72 2002–2013. They presented that the large amplitude of Q10DW-W1 is found in the  
73 ~~mid-latitude (40–50° latitude)~~ mesosphere and lower thermosphere (MLT) region of  
74 both hemispheres in equinoxes, although their results are limited to the latitude of  $50^\circ$   
75 because of the yaw cycle of the satellite. Hirooka (2000) reported that the global  
76 structure of Q10DW-W1 using the Improved Stratosphere and Mesospheric Souder  
77 (ISAMS) instrument aboard Upper Atmosphere Research Satellite (UARS) from  
78 November 1991 to May 1992. The results also showed that the Q10DW-W1 is active  
79 during equinoxes and winter at 0.1 hPa ( $\sim 65$  km). In addition, it is found that  
80 nonuniform and background zonal wind field can influence the structure of the wave in  
81 the mesosphere. The amplitude of the Q10DW-W1 is uniform or decays in the vertical

**Deleted:** high

84 near the mesopause, and it does not increase above the mesosphere, even though the  
85 critical layer is absent. Using the airglow intensities simulated by the global circulation  
86 model assimilated by the reanalysis data from ground to 30 km, Egito et al. (2017) also  
87 found that the 10-day oscillation is dominant from autumn to spring in the mid-latitude  
88 MLT region. More recently, Huang et al. (2021) investigated the Q10DW activity based  
89 on the Modern-Era Retrospective analysis for Research and Applications version 2  
90 (MERRA-2) reanalysis data. They showed that the dominant components of Q10DW  
91 are westward-propagating waves with zonal wavenumber 1 during winter and spring in  
92 the stratosphere and mesosphere and eastward-propagating waves with zonal  
93 wavenumber 1 and 2, which are excited in the mesospheric instability region. Although  
94 both westward and eastward Q10DW modes are found, they mainly focus on the  
95 eastward propagating Q10DW.

Deleted: ¶

96 Several studies have investigated the response of Q10DW-W1 to SSWs.  
97 Matthias et al. (2012) conducted a composite analysis of wave activities during major  
98 Northern Hemisphere (NH) SSWs from 1989 to 1998, revealing an amplification of  
99 Q10DW-W1 in the NH high-latitude MLT region following major SSW events. He et  
100 al. (2022a, 2022b) utilized NH MRs to observe the occurrence of Q10DW-W1 and  
101 Q16DW-W1 during four winter major SSWs. They found that these waves persisted for  
102 approximately three to five whole cycles during the events. Chandran et al. (2013)  
103 examined the forcing of secondary PWs-W1 driven by stratospheric instability on zonal  
104 winds as a response to 2012 NH minor SSW. Sassi and Liu (2014) conducted numerical  
105 simulations during minor and major NH SSWs and solar minimum condition. They  
106 found that PWs-W1 with periods between 2 and 10 days originating in the high-latitude  
107 NH could propagate equatorward and influence equatorially trapped tides. This

109 equatorward propagation of secondary PWs was also reported by Qin et al. (2022).  
110 They suggested that secondary PWs-W1 with periods of 10 to 16 days generated in the  
111 high-latitude NH during sudden stratospheric final warming could impact the Southern  
112 Hemisphere (SH) stratosphere, depending on the phase of Quasi-Biennial Oscillation  
113 (QBO). In the SH, studies by Lee et al. (2021) and Wang et al. (2021) using SH MRs  
114 reported that Q10DW was amplified prior to 2019 SH SSW. Yamazaki and Matthias  
115 (2019) reported that the Q10DW-W1 is not only intensified during SSWs but also  
116 affected by seasonal timing of SSWs (i.e., final stratospheric warming) in stratospheric  
117 instability regions.

118 While the amplification mechanism of Q10DW-W1 generated following SSWs  
119 has been addressed in previous studies (e.g., Qin et al., 2022, Yin et al., 2023), the  
120 specific mechanisms driving their seasonal amplification during equinoxes remain less  
121 explored. In the present study, we focus on the seasonal variation of Q10DW-W1 in the  
122 SH high-latitude MLT region using MRs located in Antarctica. Plus, we carry out

123 numerical simulations using the Specified Dynamics version of the Whole Atmosphere  
124 Community Climate Model (SD-WACCM) nudged towards MERRA-2 reanalysis data  
125 in order to elucidate the observed Q10DW-W1 and its amplification mechanism.  
126 Section 2 describes two MRs located in the Davis station (68.6°S, 77.9°E) and King  
127 Sejong Station (KSS; 62.2°S, 58.8°W) and how we obtain Q10DW-W1 from the  
128 observations. Also, the SD-WACCM experiments and Microwave Limb Sounder  
129 (MLS) data used for validation are described in Section 2. Results are presented in  
130 Section 3. In Section 3.1, we show seasonal variation of observed and modeled  
131 Q10DW-W1 in the SH high-latitude MLT region. The amplification mechanism of  
132 Q10DW is discussed in Section 3.2. Q10DW activities from SD-WACCM simulations

**Deleted:** not only winter

**Deleted:** Some studies have investigated the climatological and general properties of Q10DW-W1 activities in the mid- and low-latitudes, but their seasonal variation in the high-latitude MLT region has not been fully explored. In addition, the amplification mechanism of Q10DW-W1 still has not been investigated.

**Deleted:** Southern Hemisphere (SH)

140 are demonstrated in Section 3.3. In Section 4, the results are summarized, and their  
141 implications are discussed.

142

## 143 **2. Data and Method**

### 144 **2.1 Meteor Radars**

145 In this study, we use two MRs located in the Davis station (68.6°S, 77.9°E) and  
146 King Sejong Station (KSS; 62.2°S, 58.8°W), Antarctica from 2012 to 2016. The  
147 operating frequencies of both Davis and KSS MRs are 33.2 MHz and the peak powers  
148 are 6.8 kW and 12 kW, respectively. Details of the operation parameters of Davis and  
149 KSS are summarized in Holdsworth et al. (2008) and Lee et al. (2018), respectively. A  
150 large number of studies has been performed to investigate the PW or tidal activities in  
151 the MLT region with a single-station measurements of horizontal winds from an MR  
152 (e.g., Eswaraiah et al., 2019; Luo et al., 2021; Wang et al., 2021; Liu et al., 2022; Lee et  
153 al., 2021). However, single-station analysis has a limitation in diagnosing the wave  
154 propagation direction, and thus most of such studies focused on the timing of  
155 occurrence and amplitude variations of wave with a particular periodicity. For detailed  
156 analysis of PWs based on the Rossby normal modes, propagation directions and  
157 wavenumbers need to be considered. Recently, He et al. (2018) developed a method of  
158 estimating wave propagation direction and wavenumber as well as amplitude by  
159 adopting Phase Differencing Technique (PDT) to longitudinally separated MR  
160 observations based on the method of Walker et al. (2004). Since the longitude  
161 difference ( $\lambda_{\Delta}$ ) between Davis and KSS is about 137°, it is appropriate for analyzing  
162 PWs with zonal wavenumber 1 by applying the PDT. In order to estimate the zonal

163 wavenumber ( $s$ ), we first make a continuous wavelet transform from the daily-mean  
164 Davis and KSS MRs data ( $W_{(f,t)}^{Davis}$ ,  $W_{(f,t)}^{KSS}$ ), respectively, using [the](#) Morlet wavelet  
165 function as a mother wavelet function (Torrence and Compo, 1998). Then, [the](#) cross  
166 wavelet spectrum  $C_{(f,t)}$  is derived:  $C_{(f,t)} = W_{(f,t)}^{*Davis} W_{(f,t)}^{KSS}$ , where \* denotes the complex  
167 conjugate. Using the phase difference ( $\theta_{\Delta}$ ) obtained from  $\theta_{\Delta} = \text{Arg}(C_{(f,t)})$  at a given  
168 frequency and time, we estimate zonal wavenumber ( $s$ ):  $s = (-\theta_{\Delta}/(2\pi) + C)/\lambda_{\Delta}$ . In  
169 this study, we focus on the PW activity with  $s = 1$ , and the number of whole wave cycle  
170 ( $C$ ) between two stations is set to be zero (see He et al., 2018 for detailed PDT analysis).

171 Classical wave theory shows that the latitudinal structures of zonal and  
172 meridional wind [components](#) for Q10DW normal mode from the Laplace tidal equation  
173 are antisymmetric and symmetric with respect to the equator, respectively (e.g., Figure 1  
174 in Yamazaki and Matthias, 2019). The magnitude of Q10DW-W1 has maxima at the  
175 latitude of 25° and poles for zonal and meridional wind components, respectively.  
176 Around the latitude of 65°S close to the latitudes of the two MR observation sites, the  
177 normalized amplitude of Q10DW-W1 normal mode for the zonal wind is nearly zero,  
178 but the normalized normal mode magnitude for the meridional wind is larger than the  
179 half of the maximum magnitude for the meridional wind (Yamazaki and Matthias,  
180 2019). For this reason, daily-mean meridional wind data from the MRs is used for the  
181 Q10DW analysis.

182

## 183 2.2 SD-WACCM

184 In this study, for detailed analysis of the observed Q10DW-W1 activity and its  
185 amplification mechanism, we compare observational results with Q10DW-W1

Deleted: wind



187 simulated using the Specified Dynamics (SD) version of WACCM version 4 (Marsh et  
188 al., 2013). WACCM4 is a high-top (up to the lower thermosphere about 140 km)  
189 atmospheric component model of the Community Earth System Model developed at the  
190 National Center for Atmospheric Research. WACCM4 employs Community  
191 Atmospheric Model (CAM) version 4 physics package. The default horizontal  
192 resolution of WACCM4 is  $1.9^{\circ} \times 2.5^{\circ}$  (lat.  $\times$  long.), and it uses the 88 hybrid sigma  
193 vertical levels for the SD mode. Since we focus on the PWs such as Q10DW-W1, daily-  
194 mean values from the SD-WACCM are used. In this study, two SD-WACCM  
195 experiments with two different nudging depths (EXP60 and EXP75) are performed. In  
196 the EXP60 and EXP75, model variables are nudged towards the MERRA-2 reanalysis  
197 data from surface to about 60 km in altitude and 75 km, respectively. The MERRA-2  
198 reanalysis is produced by assimilating various types of observations into the Goddard  
199 Earth Observing System version 6 (GEOS-6) global model (Gelaro et al., 2017). In  
200 addition to conventional meteorological observations and operational satellite  
201 measurements, the Earth Observing System (EOS) Aura MLS temperature and ozone  
202 data are included in the assimilation procedure of the MERRA-2 from 5 hPa (~37 km)  
203 up to 0.02 hPa (~75 km) and from 250 hPa (~10 km) to 0.1 hPa (~65 km), respectively  
204 (Gelaro et al., 2017; McCormack et al., 2021). There is a divergence damping layer near  
205 the top boundary of the GEOS-6 model used for production of the MERRA-2 reanalysis,  
206 (Fujiwara et al., 2017). The divergence damping is often used to effectively and  
207 selectively remove high-frequency (noisy) gravity waves keeping the large-scale  
208 circulation and PWs structure less changed (Jablonowski and Williamson, 2011). As a  
209 result, MERRA-2 reanalysis can reflect the large-scale MLT variabilities (e.g.,  
210 McCormack et al., 2021; Harvey et al., 2021). As suggested by Brakebusch et al.

**Deleted:** above

**Deleted:** 5 hPa (~37 km)

**Deleted:** , but the use of the sponge is based on the divergence damping in the MERRA-2

**Deleted:** see

**Deleted:** ; <https://www.sparc-climate.org/sparc-report-no-10>

217 (2013), nudging coefficients for EXP60 and EXP75 are  $0.01 \text{ s}^{-1}$  below the altitudes of  
218 50 km and 65 km, respectively, and they linearly decrease and become zero above the  
219 altitudes of 60 km and 75 km, respectively.

220 WACCM simulation requires the data of sea surface temperature, sea ice  
221 fraction, solar and geomagnetic indices, and ionization rate by energetic particle  
222 precipitation (EPP) for the time period of simulations. The sea surface temperature and  
223 sea ice fraction data are produced by the NOAA Optimum Interpolation (Reynolds et  
224 al., 2002). The solar and geomagnetic indices are obtained from NASA GSFC/SPDF  
225 OMNIWeb interface (<https://omniweb.gsfc.nasa.gov/ow.html>). The EPP ionization rate  
226 is provided by the CCM1 reference-C2 data for the period of 1960–2100 (Eyring et al.,  
227 2013). Regarding MLT dynamics, effects of gravity wave drag (GWD) are crucial.  
228 WACCM includes a suite of GWD parameterizations (Richter et al., 2010) for effects of  
229 unresolved GW momentum transfer from orography (McFarlane, 1987), deep  
230 convection (Beres et al., 2005), and frontal activity (Charron and Manzini, 2002). SD-  
231 WACCM simulations start from January 1, 2011 and end at the end of 2016. First one-  
232 year results are discarded as a spin-up, and results for 2012–2016 are compared with  
233 MR observations.

234

### 235 **2.3 MLS**

236 For validation of Q10DW-W1 estimates obtained from MR observations, we  
237 derive the geostrophic winds from geopotential height (GPH) data (version 5.1 product)  
238 measured using MLS onboard the NASA's EOS Aura satellite (Schwartz et al., 2008).  
239 Geostrophic wind components are computed following Matthias and Ern (2018). The

240 Aura satellite launched on July 2004 is in a sun-synchronous orbit with an altitude of  
241 705 km. Spatial coverage of MLS instrument is from 82°S to 82°N with a 165 km  
242 resolution along the track. The sun-synchronous orbit of Aura satellite can provide a  
243 global coverage data per day with about 15 orbits. The global coverage of GPH is  
244 produced using daily mean values in 5°×5° (lat. × long.) grids. In this process, GPH  
245 data is filtered on the basis of the recommended precision, status, quality, and  
246 convergence thresholds of Version 5.0 Level 2 and 3 data quality and description  
247 document ([https://mls.jpl.nasa.gov/data/v5-0\\_data\\_quality\\_document.pdf](https://mls.jpl.nasa.gov/data/v5-0_data_quality_document.pdf)).  
248

### 249 **3. Results and Discussion**

#### 250 **3.1 Seasonal variation of Q10DW-W1 in the MLT region**

251 The perturbation meridional wind for Q10DW-W1 is symmetric in latitude  
252 about the equator as mentioned earlier. Therefore, in order to extract and analyze  
253 Q10DW-W1, which is potentially related to the Rossby normal mode in the MLT  
254 region, it is necessary to confirm whether the latitudinal structure of Q10DW-W1 has  
255 the hemispheric symmetry. Although the KSS and Davis MR observations can provide  
256 information about the longitudinal propagation of Q10DW-W1, it is impossible to  
257 estimate the latitudinal structure using these radars alone. In this study, the meridional  
258 geostrophic winds obtained from the MLS geopotential data are used to confirm the  
259 hemispheric symmetry of Q10DW-W1 estimated from MRs. The amplitudes of  
260 Q10DW-W1 in the MLS are obtained using the two-dimensional Fast Fourier transform  
261 (FFT) of the geostrophic meridional winds averaged over the height range of 80–90 km  
262 in time (30-day sliding window) and longitude domain. The time-latitude cross section

263 of the amplitude of Q10DW-W1 derived from the MLS geostrophic meridional wind  
264 averaged over the height range of 80–90 km is presented in the Supplement (Fig. S1).  
265 Hereafter, the Q10DW denotes westward-propagating quasi-10-day normal mode wave  
266 with zonal wavenumber 1 and the hemispheric symmetry, where quasi-10-day  
267 periodicity means the periods between 9 and 11 days. Unless the hemispheric symmetry  
268 is satisfied, the analyzed westward propagating signals with zonal wavenumber 1 are  
269 referred to as quasi-10-day-like oscillations (Q10DOs).

270 Figure 1 shows the time-height distributions of the amplitudes of Q10DWs and  
271 Q10DOs derived from the daily-mean meridional winds observed at the Davis and KSS  
272 MRs using the PDT method. The regions shaded in gray represent the time periods  
273 when the hemispheric symmetry is not found in the MLS results as shown in Fig. S1.  
274 The time periods of the hemispheric symmetries are defined by the periods when the  
275 amplitudes of the MLS meridional geostrophic winds (vertically averaged over 80–90  
276 km) with quasi-10-day periodicity exceed  $3.5 \text{ m s}^{-1}$  in both  $60^\circ\text{N}$ – $80^\circ\text{N}$  and  $60^\circ\text{S}$ – $80^\circ\text{S}$ .  
277 The MLS results in solstices are generally shaded in gray (see Fig. S1). This result  
278 indicates that Q10DWs in a form of normal modes are found during equinoxes, which is  
279 consistent with the results from Forbes and Zhang (2015). Using the periods of the  
280 hemispheric symmetry of the Q10DW obtained from the MLS, we identify the normal  
281 mode Q10DW from the Davis and KSS MR observations.

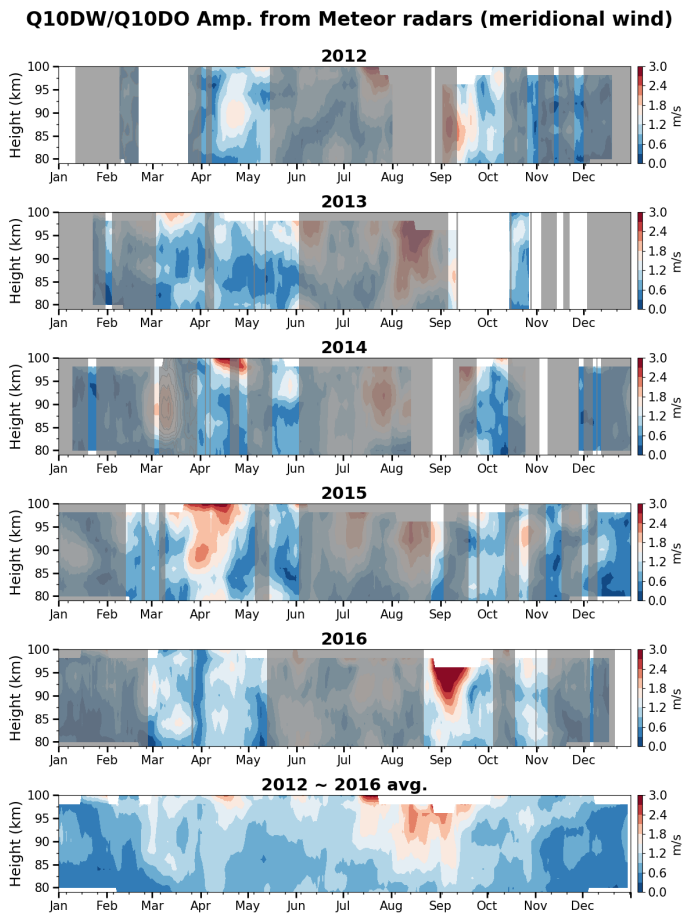
282 The 5-yr average (The bottom-most panel of Fig. 1) between 2012 and 2016  
283 indicates that the Q10DWs are generally enhanced from late February to April and from  
284 late August to September in the altitude range of 82–98 km with the maximum  
285 amplitude of  $2.6 \text{ m s}^{-1}$ . The Q10DWs are usually more amplified in early spring from  
286 late August to September with the largest amplitudes around the altitudes of 90–95 km.

Deleted: 27.2

288 Large amplitudes are found in winter (July to mid-August), but they are unlikely to  
289 represent the normal mode Q10DWs, as it is clear from the gray shading in winter.  
290 According to Wang et al. (2021), the nonlinear wave-wave interaction can generate  
291 Q10DOs in southern winter. Their Q10DOs are eastward propagating, interacting with  
292 stationary PWs with zonal wavenumber 1. Meanwhile, the Q10DWs and Q10DOs (Fig.  
293 1) obtained from two MRs using the PDT method are westward propagating.  
294 Understanding of the mechanisms of the winter-time westward-propagating Q10DOs is  
295 beyond the scope of this study, and it requires continuing researches.

296 For individual years, it is also found that the amplitude of Q10DW is generally  
297 large in equinoxes (see panels for each year in Figs. 1 and S1). During March–April  
298 (autumn), active Q10DWs are identified, and their amplitudes reach up to  $\sim 3$  m s<sup>-1</sup> in  
299 2014 and 2015. Particularly, the peak in September (spring) is prominent in 2016. These  
300 MR observation results are remarkably consistent with results obtained using satellite  
301 geopotential height in the SH high-latitude region (Forbes and Zhang, 2015).  
302 Occasionally, large amplitude Q10DWs are observed near the altitude of 98–100 km in  
303 equinoxes (e.g., April 2015), but results around 100 km can be less reliable because the  
304 number of MR echoes above 96 km is much smaller than that around 90 km (Lee et al.,  
305 2022).

Deleted: 33



307

308 **Figure 1.** Time-height distributions of the amplitudes of Q10DWs (unshaded region)  
 309 and Q10DOs (shaded region) derived from meridional winds observed by MRs at Davis  
 310 [\(68.6°S, 77.9°E\)](#) and KSS [\(62.2°S, 58.8°W\)](#) for 2012–2016. The bottom-most panel  
 311 shows the 5-yr average from 2012 to 2016. The gray shading represents time periods  
 312 where the hemispheric symmetry is unclear in the MLS results [\(see the text for details](#)  
 313 [of the unclearness of symmetry\)](#).

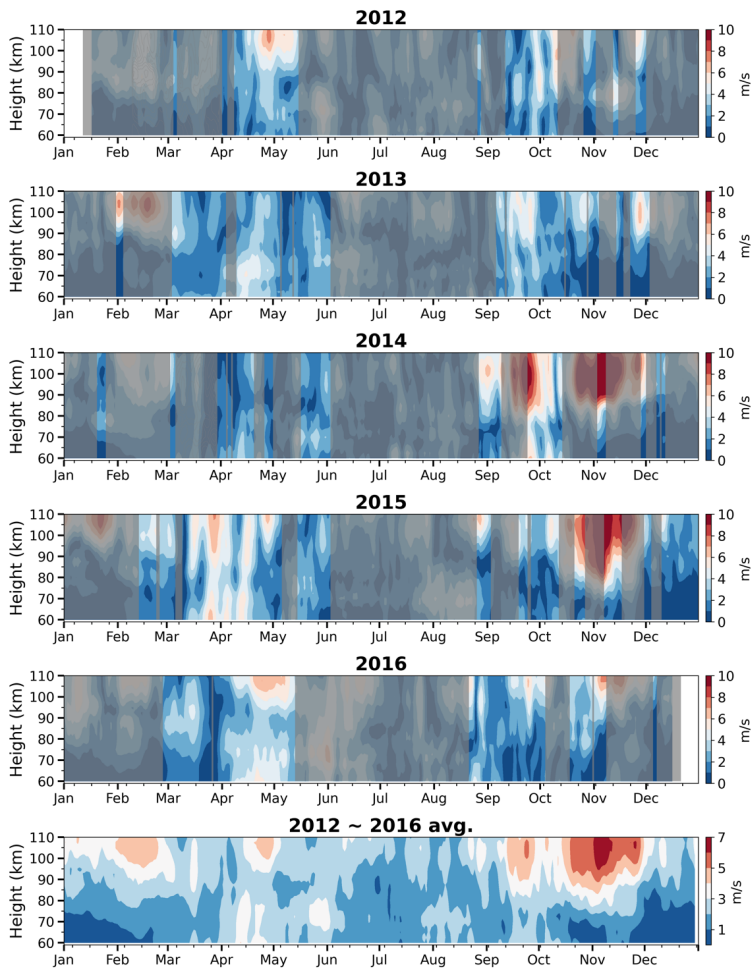
Deleted: .

315 Figure 2 demonstrates the time-height distributions of the amplitudes of  
316 Q10DWs and Q10DOs around the latitude of 63°S in the EXP75 SD-WACCM  
317 simulation for the altitude range of 60–110 km for 2012–2016, along with the  
318 hemispheric symmetry period obtained from the MLS results. The bottom-most panel of  
319 Fig. 2 shows the 5-yr average from 2012 to 2016. The amplitudes are obtained by  
320 decomposing the meridional winds obtained from the simulation into westward  
321 propagating Fourier modes with zonal wavenumber 1 using the 2D FFT in time (30-day  
322 sliding window) and longitude domain around 63°S. From Fig. 2, it is clear that the  
323 seasonal variations of Q10DW amplitudes obtained from the simulation have year-to-  
324 year variations, as in the Q10DW amplitudes derived from the two MRs. However, the  
325 Q10DW activities observed from the MR observations are generally larger than those in  
326 the EXP75 simulation (see Fig. 1).

327 The 5-yr average in Fig. 2 shows that there are four main time periods  
328 (February, April, September, November) when the modeled Q10DWs and Q10DOs are  
329 active in the EXP75. The time periods of April and September are consistent with the  
330 MR observations in terms of Q10DW amplitudes and the hemispheric symmetry  
331 obtained from the MLS, but the other periods are not. The active signals simulated in  
332 February and November do not appear to be normal mode Q10DWs because the  
333 hemispheric symmetry is not seen in the MLS data during February and November. For  
334 a more comprehensive understanding of the Q10DOs in the EXP75 during February and  
335 November, we will discuss in more detail later in Section 3.3 by comparing between the  
336 EXP75 and EXP60.

Deleted: in

**Q10DW/Q10DO Amp. from EXP75 (meridional wind) at 63S**

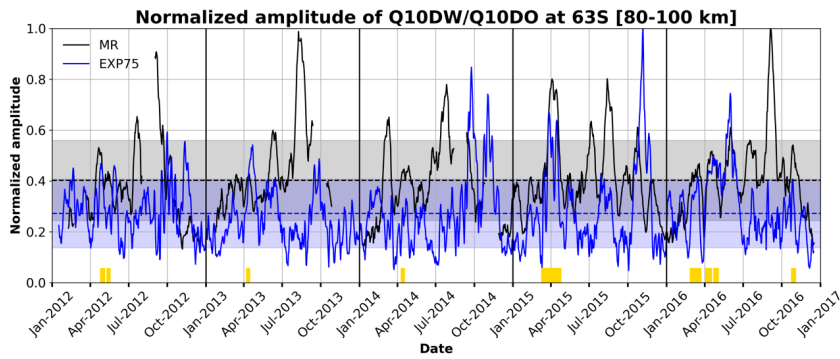


338

339 **Figure 2.** Time-height distributions of the amplitudes of Q10DWs (unshaded region)  
340 and Q10DOs (shaded region) around 63°S for 2012–2016 in the EXP75. The bottom-  
341 most panel shows the 5-yr average between 2012 and 2016. The gray shaded areas  
342 represent periods where the hemispheric symmetry is not observed in the MLS results.



343 Figure 3 shows time series of the normalized amplitudes of Q10DWs and  
344 Q10DOs obtained from the MR observations (black) and EXP75 simulation (blue).  
345 Normalization is carried out by averaging the amplitudes in the altitude range between  
346 80 and 100 km and dividing the 5-yr averaged values by the respective maximum  
347 values in the same altitude range. We select the dates when (i) the amplitudes obtained  
348 from both MRs and EXP75 exceed their respective 5-yr mean values, (ii) their  
349 correlation is relatively large ( $> 0.6$ ), and (iii) the hemispheric symmetry occurs in the  
350 MLS results. The correlation coefficients are computed for sliding 7-day windows with  
351 1-day step. The dates when the three criteria are satisfied are represented by yellow  
352 boxes on abscissa in Fig. 3. The total number of the dates when the Q10DW was  
353 substantially active in both observations and model (EXP75) is 46. Using EXP75 results  
354 on the selected dates, the amplification mechanisms of the observed Q10DW will be  
355 discussed.



356

357 **Figure 3.** Time series of normalized amplitudes of Q10DW/Q10DOs from the  
 358 observations (black line) and EXP75 simulation (blue line). The dashed lines and  
 359 shaded areas represent the mean and standard deviation of normalized amplitude of  
 360 Q10DW/Q10DOs from the observations (black) and EXP75 (blue), respectively.  
 361 Yellow boxes on abscissa indicate the dates when the normalized amplitudes from both  
 362 MRs and EXP75 can be considered to be due to the normal mode Q10DWs.

Deleted: those of

### 364 3.2 Amplification mechanisms of Q10DW

365 The amplitude of upward propagating PWs grows with height when their  
366 vertical propagation is allowed, but it can decrease with height in the evanescent region  
367 where the square of refractive index  $n^2$  becomes negative. Regions of negative  $n^2$  are  
368 often accompanied by regions of the negative latitudinal gradient of zonal-mean  
369 potential vorticity ( $q_\phi$ ), where  $q$  is the zonal-mean quasi-geostrophic potential vorticity  
370 (QGPV), the overbar denotes zonal averaging,  $\phi$  is the latitude, and the subscript  $\phi$   
371 denotes the partial derivative in the latitudinal direction. In the regions of negative  $q_\phi$ ,  
372 the barotropic and baroclinic instabilities can occur (Matsuno, 1970), and it is known  
373 that PWs can amplify extracting energy from the mean flow while they pass through the  
374 instability regions (Meyer and Forbes, 1997; Cohen et al., 2013). If PWs somehow  
375 reach their critical lines within an instability region, it is possible for these PWs to  
376 tunnel through the critical lines (Rhodes et al., 2021). In case that the evanescent region  
377 is thin enough, and the PWs can reach their critical lines, it is also possible for the  
378 overreflection to take place, resulting in the amplified PWs and the propagation of the  
379 amplified PWs out of the overreflection region (Lindzen et al., 1980; Rhodes et al.,  
380 2021).

381 Another possible way of modulating PWs is their excitation by the  
382 nonconservative GW forcing (Song et al., 2020). Nonconservative GWD forcing  
383 (NCGWD;  $Z'$ ) can generate PWs as it is clearly seen from the perturbation QGPV  
384 equation given in the form of wave action conservation equation (1) when diabatic  
385 forcing is ignored in  $Z'$  [see Andrews et al. (1987) and Palmer (1982) for details]:  
386

Deleted: -

Deleted:

$$389 \quad \frac{\partial A}{\partial t} + \nabla \cdot \mathbf{F} = \rho_0 \overline{Z' q'_{(M)}} / (q_\phi / a), \quad (1)$$

390

391 where  $a$  is the earth's mean radius;  $\rho_0$  is the reference density given as an exponentially  
 392 decreasing function of log-pressure height  $z$ ; the prime denotes the perturbation from the  
 393 respective zonal mean;  $A$ , defined below using  $q'_{(M)}$ , is the wave-activity density in the  
 394 spherical QG system;  $q'_{(M)}$  is the perturbation of modified QGPV, modified to consider  
 395 the planetary vorticity advection by the isallobaric meridional wind in spherical geometry  
 396 (Matsuno, 1970; Palmer, 1982);  $Z'$  is the curl of the horizontal GWD perturbation;  $\nabla \cdot \mathbf{F}$   
 397 is the divergence of Eliassen-Palm (EP) flux ( $\mathbf{F}$ ), and the flux  $\mathbf{F}$  is considered to be the  
 398 wave-activity flux given by  $\mathbf{F} = \mathbf{c}_g A$  in the QG framework, where  $\mathbf{c}_g$  is the group velocity  
 399 in the latitude-height domain.

400 In (1), the wave-activity density  $A$  and the modified QGPV perturbation  $q'_{(M)}$  are  
 401 given in spherical geometry (Palmer, 1982), respectively, as follows:

402

$$403 \quad A = a \cos \phi \frac{1}{2} \rho_0 \frac{\overline{q'^2_{(M)}}}{q_\phi / a}, \quad (2)$$

$$404 \quad q'_{(M)} = \frac{v'_\lambda}{a \cos \phi} - \frac{f}{a \cos \phi} \left( \frac{u' \cos \phi}{f} \right)_\phi + \frac{f}{\rho_0} \left( \rho_0 \frac{\theta'}{\theta z} \right)_z, \quad (3)$$

405

406 where  $u$  and  $v$  are zonal and meridional wind components, respectively;  $\lambda$  is the  
 407 longitude;  $f$  is the Coriolis parameter;  $\theta$  is the potential temperature. The subscript  $\lambda$  and  
 408  $z$  mean the partial derivatives in longitude and vertical directions, respectively.

Deleted: Where

410 For understanding of amplification of PWs around the instability regions, the  
 411 barotropic and baroclinic instability regions are determined by the negative sign of  $q_\phi$   
 412 (Andrews et al. 1987) given by:

413

$$414 \quad q_\phi = 2\Omega \cos \phi - \left[ \frac{(\alpha \cos \phi)_\phi}{\alpha \cos \phi} \right]_\phi - \frac{\alpha}{\rho_0} \left( \frac{\rho_0 f^2}{N^2} \mathbf{u}_z \right)_z, \quad (4)$$

415

416 where  $\Omega$  is the earth's rotation rate and  $N$  is the buoyancy frequency. The negative sign  
 417 of  $q_\phi$  is a necessary condition of the barotropic and baroclinic instabilities. The second  
 418 (with negative sign) and third (with negative sign) terms on the right-hand side of (4)  
 419 represent the meridional and vertical curvatures of the zonal-mean zonal wind,  
 420 respectively. If the second or third term is dominant,  $q_\phi$  can become negative, and the  
 421 instabilities can take place.

422 The square of refractive index  $n^2$  is used to analyze the propagation  
 423 characteristics of PWs and depends on the mean QGPV gradient as follows:

424

$$425 \quad n^2 = \frac{q_\phi}{\alpha(u-c)} - \frac{s^2}{\alpha^2 \cos^2 \phi} - \frac{f^2}{4N^2 H^2}, \quad (5)$$

426

427 where  $c$  is the zonal phase speed of single PW (i.e.,  $c = 2\pi a \cos \phi / (s\tau)$ ;  $s$  is the zonal  
 428 wavenumber, and  $\tau$  is the wave period), and the constant scale height  $H$  is set equal to 7  
 429 km. The propagation of PWs is possible in regions of positive  $n^2$ . On the other hand,  
 430 PWs can be reflected or be evanescent in the region where  $n^2 < 0$  (Matsuno, 1970).

431 In order to analyze the wave propagation and wave activity for the selected dates  
 432 for Q10DWs (or Q10DOs) found in MRs and model simulations, we use the EP flux as  
 433 diagnostic tools, derived in the Transformed Eulerian-Mean framework for the spherical  
 434 QG system (Palmer, 1982; Andrews et al., 1987). In the spherical geometry, the  
 435 meridional  $F^{(\phi)}$  and vertical  $F^{(z)}$  components of the EP flux  $\mathbf{F} \equiv [0, F^{(\phi)}, F^{(z)}]$  are  
 436 given by

$$438 \quad F^{(\phi)} = -\rho_0 a \cos \phi \bar{u}^r \bar{v}^r, \quad (6)$$

$$439 \quad F^{(z)} = \rho_0 a \cos \phi f \bar{v}^r \bar{\theta}^r / \theta_z, \quad (7)$$

440

441 Figure 4 shows the EP flux  $\mathbf{F}$  and wave activity density normalized by  $\rho_0 a \cos \phi$   
 442 for Q10DWs in the EXP75. The propagation inhibition region ( $n^2 < 0$ ) and the  
 443 contours of zonal-mean zonal wind are overplotted. Thick green and black lines indicate  
 444 the regions of  $q_\phi = 0$  and of critical lines for Q10DWs, respectively. The critical lines  
 445 are plotted by computing the zonal phase speed ( $c$ ) of Q10DW:  $c = 2\pi a \cos \phi / (s\tau)$ ,  
 446 where  $s = 1$  and  $\tau = 10$  day. The wave-activity density is shaded in blue and red  
 447 depending on its sign  $[\text{sgn}(A)]$ . For the EP flux vector,  $\mathbf{F}/\text{sgn}(A)$  ( $= \mathbf{c}_g |A|$ ), rather than  
 448  $\mathbf{F}$  itself ( $= \mathbf{c}_g A$ ), is plotted such that the EP flux can always be parallel to the local  
 449 group velocity of Q10DWs regardless of the instability regions where  $q_\phi < 0$  and thus  
 450  $A < 0$ . For better illustration of the EP flux in the atmosphere where its density  
 451 decreases exponentially with height, the meridional and vertical components of EP flux

Deleted: ( )  
 Deleted: ( )  
 Deleted: ( )  
 Deleted: ( )  
 Deleted: ( )  
 Deleted: ( )

458 are scaled by  $(p_s/p)^{0.85}[F^{(\phi)}/(a\pi), F^{(z)}/(3 \times 10^5)]$  (Edmon et al., 1980; Gan et al.,  
459 2018), where  $p_s$  and  $p$  are the surface and atmospheric pressures, respectively.

460 For Fig. 4, we select the four dates of (a) 30 April 2012, (b) 11 April 2013, (c) 6  
461 April 2015, and (d) 29 October 2016 when the three criteria mentioned in Fig. 3 are  
462 satisfied (see yellow boxes in Fig. 3). That is, the normalized amplitudes of Q10DWs  
463 from both MRs and EXP75 are larger than its average, the correlation coefficient is  
464 larger than 0.6, and the hemispheric symmetry is found in the MLS results. The 30  
465 April 2012 case (Fig. 4a) shows that the stratospheric jet is located around (40°S–60°S,  
466 55 km) in the latitude-height domain and that there is a predominant branch of upward  
467 and equatorward Q10DW EP flux vectors across the center of the stratospheric jet. In  
468 the high-latitude mesosphere, there are two regions where both the large-scale  
469 instability ( $q_\phi < 0$ ) and evanescence ( $n^2 < 0$ ) take place, and they are located in  
470 (55°S–65°S, 60–85 km) and (65°S–80°S, 70–110 km), respectively. Along the  
471 instability boundaries (green lines), large positive or negative Q10DW activities are  
472 found. Divergent EP flux vectors in the meridional direction are clearly seen around the  
473 instability region located at (53°S, 65–75 km), which implies the excitation of Q10DWs  
474 in association with the instability. In the region of MR observations (60°S–65°S, 85–  
475 100 km), substantially amplified Q10DW activity appears, and the equatorward  
476 Q10DW EP flux towards the MR sites is found over the amplified Q10DW activity.

477 Figure 4b demonstrates the case of 11 April 2013. One major branch of Q10DW  
478 EP flux vectors (Fig. 4b) originates from the stratospheric jet located at (55°S–60°S,  
479 45–60 km). In the southern and upper side of the stratospheric jet, the instability and  
480 evanescent region extends from 45 km to 70 km height in the latitude of 50°S–75°S.

Deleted: Figure

Deleted: s

483 Above the instability region, distinct region of strong wave activity is found around  
484 (50°S–65°S, 65–90 km), and this region is partially overlapped by the MR observation  
485 region. Around this region, the Q10DW EP flux is directed downward and poleward  
486 inside of the instability region (within green line). The Q10DW EP flux is directed  
487 upward and equatorward outside and above the instability region. This diverging pattern  
488 of EP flux around the instability region also shows the possibility of the excitation of  
489 Q10DW in association with the instability.

490 For 6 April 2015 case (Fig. 4c), the structure of wave-activity density and  
491 instability regions are similar to the 30 April 2012 case (Fig. 4a). The instability and  
492 evanescent regions occur around (60°S–80°S, 70–100 km). Along the instability  
493 boundaries, there are strong positive and negative wave-activity densities, and this  
494 region of strong wave activities includes the MR observation region. Again, the  
495 divergence of Q10DW fluxes appears in the upper part of the instability region around  
496 (60°S–70°S, 80–100 km). The Q10DW propagates upward and equatorward outside of  
497 the instability region and downward inside of the instability region, as in the other dates  
498 shown in Figs. 4a and 4b. Unlike the other events, the propagation of Q10DW is  
499 poleward in the stratosphere (30–60 km altitude). This result is consistent with Qin et al.  
500 (2022). They reported that the meridional component of EP flux extends from the  
501 stratosphere in the NH across the equator to the SH stratosphere during the westerly  
502 phase of QBO in the middle stratosphere and during the westerly phase of the semi-  
503 annual oscillation in the upper stratosphere.

504 In 29 October 2016 case (Figure 4d), the center of stratospheric jet is located  
505 around (60°S–70°S, 20–30 km). Above the stratospheric jet, the eastward wind turns

Deleted: divergent

Deleted: eastward



508 westward around the altitude of 60 km. Within the region of westward wind, the  
509 instability and evanescent regions are found. In addition, the critical lines exist inside  
510 the instability region. The overreflection or transmission process can take place near the  
511 critical lines as we mentioned. Notably, the significantly large positive and negative  
512 wave-activity density regions are found around (45°S–70°S, 60–90 km) near the  
513 instability boundaries, and these regions are partially overlapped by the MR observation  
514 region. This result suggests that the observed amplification of Q10DW may be  
515 attributed to the overreflection process. The EP flux of Q10DW predominantly  
516 propagates upward and equatorward away from the strong wave-activity region around  
517 (60°S, 60–70 km) with weak poleward propagation of Q10DW towards the instability  
518 region across the critical lines.

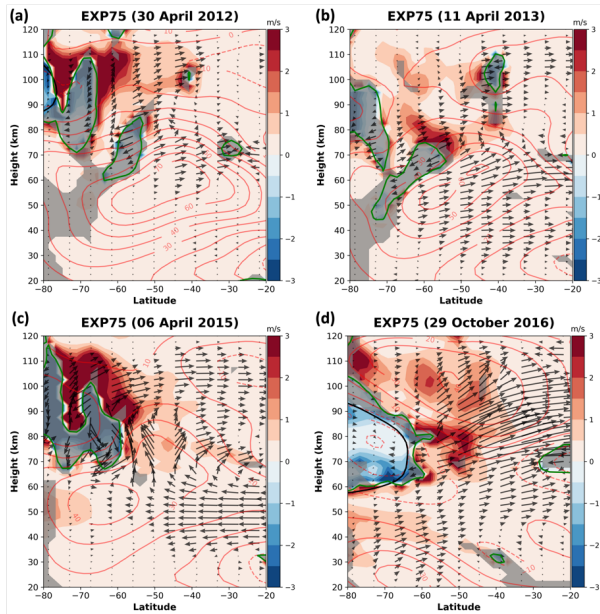
519 For all the cases shown in Fig. 4, the results indicate that a distinct strong wave-  
520 activity density region is located within the area observed by the MRs (around 60°S–  
521 70°S and 80–100 km in height), associated with the large-scale instability region.  
522 Considering the wave-activity density  $A$  is directly proportional and inverse  
523 proportional to the  $\overline{q'^2}$  and  $q_\phi$ , respectively, it can be thought that the small  $q_\phi$   
524 contributes the large magnitude of  $A$  near the instability region. However, we confirm  
525 that the large  $\overline{q'^2}$  is located around the instability region, leading to the overall large  
526 wave-activity density (not shown in here). In addition, the group velocity of the wave is  
527 given by  $\mathbf{c}_g = \mathbf{F}/A$ . For the selected cases (Fig. 4), the EP flux  $\mathbf{F}$  in the MR observation  
528 region is relatively small, while the magnitude of  $A$  is comparatively large. This  
529 suggests a small group velocity in this region. These results agree with the study of

Deleted: or transmitted

531 Thorncroft et al. (1993), which states that during the amplification of baroclinic waves,  
532 the group velocity tends to be small.

533 As previously mentioned, Song et al. (2020) proposed that the NCGWD can  
534 generate PWs. In addition, Forbes and Zhang (2015) suggested that the dissipation of  
535 gravity waves filtered by the Q10DW wind field can generate a secondary Q10DW by  
536 momentum deposition. In this regard, the both parameterized GWs and resolved GWs  
537 ( $s \geq 20$ ) could also play a role in generating Q10DW. To verify the contribution of  
538 NCGWD, we analyze linearized disturbance QGPV equation (Andrews et al., 1987) for  
539 the 4 cases shown in Fig. 4. Our analysis shows that the contribution of both NCGWD  
540 and resolved GW for the Q10DW is negligible in the MLT region (see Fig. S3 in the  
541 Supplement).

542 These results indicate that the large amplitudes of Q10DW observed in the SH  
543 high-latitude region by the Davis and KSS MRs can originate from the high-latitude  
544 stratosphere-mesosphere region, where the barotropic/baroclinic instability or  
545 overreflection near the critical layer occur.



546

547 **Figure 4.** EP flux parallel to local group velocity  $[F/\text{sgn}(A)]$  and normalized wave  
 548 activity density  $[A (\rho_0 a \cos \phi)^{-1}]$  given in the unit of  $\text{m s}^{-1}$  for the Q10DWs in the  
 549 EXP75 on (a) 30 April 2012, (b) 11 April 2013, (c) 6 April 2015, and (d) 29 October  
 550 2016. The activity density  $A$  is shaded in blue and red depending on its sign. The  
 551 boundaries of the instability regions ( $q_\phi = 0$ , green lines), the negative  $n^2$  regions (grey  
 552 shading), and the red contours for zonal-mean zonal wind are overplotted. For eastward  
 553 (westward) zonal-mean zonal wind, contours are plotted in solid (dashed) lines, and  
 554 contour interval is  $10 \text{ m s}^{-1}$ .

### 555 3.3 Comparison of Q10DO between SD-WACCM simulations

556 This section compares the Q10DOs around the mesospheric instability regions  
 557 in the two SD-WACCM simulations (EXP75 and EXP60) for February and November.

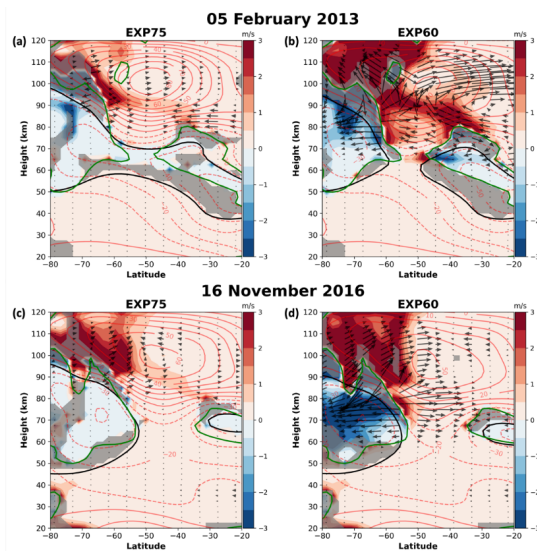
558 February and November are chosen because the amplitudes of modeled Q10DOs are  
559 substantial. The magnitude of Q10DO in the EXP75 is generally smaller than that in the  
560 EXP60, which is more comparable to the MR and MLS observations in which both  
561 Q10DWs and Q10DOs are weak (see Figs. S1 and S2 in the Supplement). Note that  
562 more realistic meteorological fields are nudged throughout the mesosphere in the  
563 EXP75. In this section, comparison between EXP75 and EXP60 for February and  
564 November is carried out to reveal mechanisms behind weak Q10DOs in the EXP75.

565 Figure 5 demonstrates the properties of Q10DO and background atmospheric  
566 conditions (as shown in Fig. 4) for 5 February 2013 and 16 November 2016 when the  
567 Q10DO activity is found to be large in both simulations. The left and right panels of  
568 Fig. 5 are the results from the EXP75 and EXP60, respectively. In Fig. 5, it is clear that  
569 the strong wave-activity density for Q10DO arise in polar regions above the altitude of  
570 70 km in the EXP60, and the magnitude of the EP fluxes in the EXP60 is **much larger**,  
571 than that in EXP75. In addition, in 5 February 2013 for the EXP60 (Fig. 5b), a  
572 substantially strong wave-activity density region is located in the mid-latitude  
573 mesospheric region as well. Around the strong wave-activity regions in the polar upper  
574 mesosphere, it is seen that the EP fluxes of Q10DWs are divergent. In addition, the  
575 distinct wave-activity density of Q10DO regions in the EXP60 occur along the  
576 instability regions and critical lines around (50°S–70°S, 70–110 km) and (20°S–40°S,  
577 65–80 km). On the other hand, the wave-activity density of Q10DO in the EXP75 (Fig.  
578 5a and 5c) is located at relatively higher altitudes (80–100 km), and the strength of  
579 Q10DO EP flux and wave-activity density are weaker than EXP60. Moreover, the  
580 negative EP flux divergence (EPFD) is much larger in the EXP60 than in the EXP75  
581 above the altitude of 80 km (not shown in here).

Deleted: Figure

Deleted: stronger

584 Our analysis reveals that the larger wave-activity density and EP fluxes in the  
 585 EXP60 along the large-scale instability region in the polar upper mesosphere compared  
 586 to the EXP75. This indicates that the stronger large-scale instability in the EXP60 can  
 587 amplify Q10DO activities, which is consistent with the analysis result that the  
 588 barotropic and baroclinic instabilities can be the major sources of the amplification of  
 589 traveling PWs (Harvey et al., 2019).

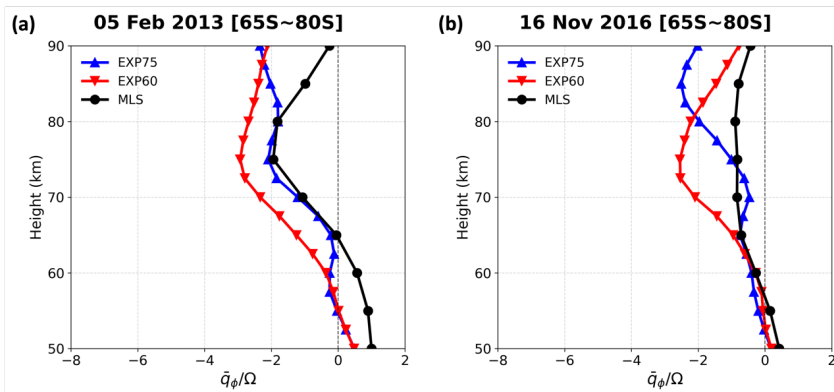


590  
 591 **Figure 5.** Same as Fig. 4 but for (a and b) 5 February 2013 and (c and d) 15 November  
 592 2016. The left and right columns represent the results from EXP75 and EXP60,  
 593 respectively.

594 Figure 6 shows the  $q_\phi$  (normalized by  $\Omega$ ) for 5 February 2013 and 16 November  
 595 2016 from the EXP75 (blue), EXP60 (red), and MLS (black). The normalization makes  
 596  $q_\phi$  dimensionless. The  $q_\phi/\Omega$  from MLS is derived in the quasi-geostrophic framework

Deleted: yellow

598 (Andrews et al., 1987) and it is included as a reference for validation. The  $q_\phi/\Omega$  is  
 599 averaged between the latitudes of 65°S-80°S where the wave-activity density is strong  
 600 and large negative  $q_\phi$  is found in Fig. 5. It is seen that the vertical profiles of  $q_\phi/\Omega$   
 601 from the EXP75 and MLS have somewhat small negative values and they are generally  
 602 similar below the altitude of 75 km, although the difference gradually increase above  
 603 the altitude of 75 km. On the other hand, large discrepancies are shown between EXP75  
 604 and EXP60 in the altitudes between 60–80 km. In the EXP60,  $q_\phi/\Omega$  has much larger  
 605 negative values, which suggest the relatively stronger barotropic or baroclinic instability  
 606 in the EXP60 and the amplification of the Q10DO in the mid-to-upper mesosphere in  
 607 association with the stronger instability in the EXP60.



608  
 609 **Figure 6.**  $q_\phi$  (normalized by  $\Omega$ ) averaged over 65°S–85°S for (a) 5 February 2013 and  
 610 (b) 16 November 2016 from the EXP75 (blue), EXP60 (red), and MLS (black).

611 The negative  $q_\phi$  can be induced by latitudinal and vertical curvatures of zonal-  
 612 mean zonal wind that correspond to the second and third terms (with negative signs) in  
 613 the right side of (4), respectively. Figure 7 shows the second (top panels) and third

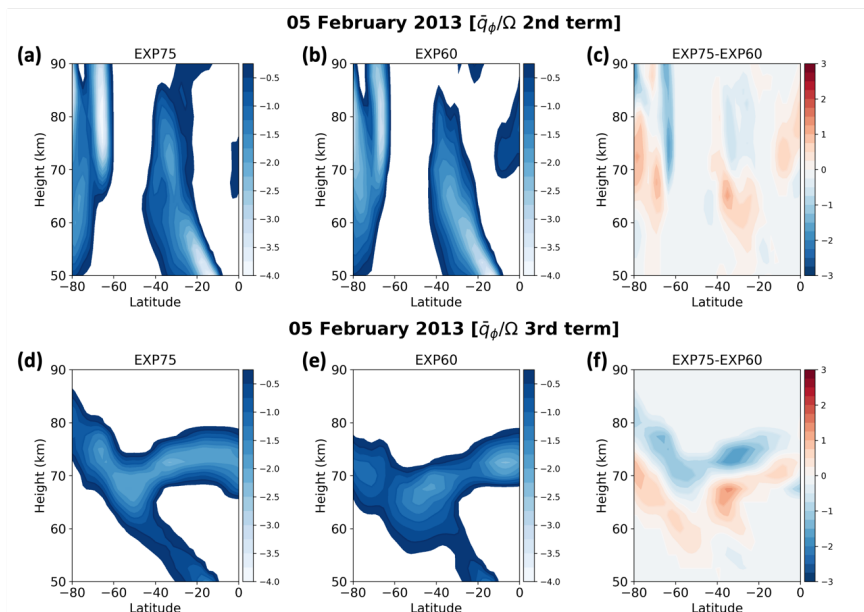
**Commented [WLee1]:** Revise the color schemes according to the Coblis – Color Blindness Simulator (<https://www.color-blindness.com/coblis-color-blindness-simulator/>).

**Deleted:** yellow

615 (bottom panels) terms, respectively, for 5 February 2013. The differences shown in  
616 Figs. 7c and 7f indicate that the larger negative  $q_\phi$  is located in the lower altitudes in the  
617 EXP60 than in EXP75, inducing the larger instability at 65–75 km in height around  
618 70°S–80°S in the EXP60, which is consistent with Fig. 6. Note that the positive  
619 differences seen at about 65–75 km in the high-latitude regions in Figs. 7c and 7f mean  
620 the larger negative  $q_\phi$  in the EXP60. Also, it is clear that both vertical and horizontal  
621 shear contribute the stronger barotropic/baroclinic instability in the EXP60 in the mid-  
622 to-upper mesosphere, as shown in Figs. 7a-b and 7d-e. This analysis demonstrates the  
623 mesospheric dynamics specified by the MERRA-2 data up to the altitude of 75 km  
624 reduces the large-scale instability in the mid-to-upper mesosphere in the EXP75. This is  
625 consistent with Sassi et al. (2021) proposed the absence of specification of middle  
626 atmosphere dynamics induce the instability in summer mesospheric westward jet,  
627 leading large traveling PWs.

628 The wind structure in the MLT region is mainly driven by momentum  
629 deposition from PWs and GWs. Harvey et al. (2019) reported that GWs can change  
630 significantly the vertical shears, leading enhanced instability and larger traveling PWs in  
631 the mesospheric region based on the satellite observations and SD-WACCM  
632 simulations. GW forcing is one of the main factors to maintain the necessary conditions  
633 of barotropic/baroclinic instability in the modeled mesosphere (Sato et al., 2018).  
634 Therefore, in order to better understand the mechanisms underlying the discrepancies in  
635 zonal wind fields and the resulting instability in the model, it is important to examine  
636 the contribution of resolved wave forcing (EPFD) and GWD forcing on the zonal wind  
637 structure in the mesosphere.

**Deleted:** In addition, the unresolved



639

640 **Figure 7.** Contributions of (top) the meridional variation of the zonally-averaged mean  
 641 flow and (bottom) its vertical variation to the instability condition (negative  $q_\phi$ ) shown  
 642 in (2), respectively, for 5 February 2013. Panels in each column present the results from  
 643 (a and d) the EXP75, (b and e) the EXP60, and (c and f) difference between EXP75 and  
 644 EXP60, respectively. Only negative values are plotted except for two panels for  
 645 difference.

646 Figure 8 shows the latitude-height distributions of zonal-mean zonal wind, zonal  
 647 component of GWD and resolved wave forcing (EPFD) in 5 February 2013 for the  
 648 EXP75, the EXP60, and the difference between EXP75 and EXP60 (EXP75-EXP60).  
 649 The zonal-mean zonal wind, zonal component of GWD, and resolved wave forcing  
 650 (EPFD) are calculated through the 21-day averaging (central date  $\pm 10$  days). For GWD,  
 651 the orographic and nonorographic values are added. In Figs. 8a-b, zero-wind lines are

Deleted: in  
 Deleted: E  
 Deleted: s



655 located around 80 km height in the SH mid-latitude region, indicating the reversal of the  
656 zonal-mean zonal wind due to the eastward momentum forcing from the GWs and  
657 resolved waves. It is clear that the zero-wind line in the EXP60 is located at lower  
658 altitudes by about 5 km compared to the EXP75, which means that eastward GWD and  
659 eastward EPFD from the EXP60 can be larger below the altitude of ~80 km than that  
660 from EXP75. Indeed, the difference field between EXP75 and EXP60 for GWD (Fig.  
661 8f) shows that the eastward GWD from the EXP60 is larger around (60°S, 70 km) than  
662 that from EXP75 as indicated by the negative difference field in those regions. In  
663 addition, the resolved wave forcing (EP flux divergence) is more eastward above the  
664 altitude of 70 km in the mid-to-high latitude regions in the EXP60 than in the EXP75.  
665 This result indicates that the eastward resolved wave forcing also contributes more in  
666 the mid-to-upper mesosphere in the EXP60, resulting in the zonal-mean zonal wind  
667 reversal (westward to eastward wind) in the lower altitude in the EXP60, as shown  
668 around 60°S in Fig. 8b.

669 As mentioned before, the amplification or modulation of westward-propagating  
670 PWs with zonal wavenumber 1 and a quasi-10-day period due to NCGWD and resolved  
671 GW is negligible (Fig. S3 in Supplement), indicating that the amplification of Q10DW  
672 or Q10DO is mainly related to the baroclinic/barotropic instability. The stronger  
673 instability in the EXP60 around the altitude of 70 km indicates that WACCM simulates  
674 a large meridional and vertical variation of zonal winds compared to the observations in  
675 the mid-to-upper mesosphere, which is likely due to the stronger eastward GWD and  
676 eastward EPFD forcing near 70 km altitude in the EXP60, as shown in Fig. 8. Cohen et  
677 al. (2013) reported that parameterized GWs can generate instability that can generate

678 resolved waves of which forcing (i.e., EPFD) can compensate GWD. Our results show  
679 that the increased eastward GWD at 70 km altitude generates instability and it leads  
680 more Q10DO. The EPFD in the EXP60 gives the more eastward forcing above 70 km  
681 enhancing the wind reversal in the mid-to-high latitudes. ~~However,~~ comparison of Figs.  
682 8f and 8i indicates that the ~~structures of GWD and EPFD are roughly 90°–180° shifted,~~  
683 in the vertical direction, ~~approximately consistent with the compensation between GWD~~  
684 ~~and EPFD.~~ Raising the nudging altitude of MERRA-2 reanalysis data to 75 km from 60  
685 km reduces the instability in the mid-to-upper mesosphere, leading to decreased the  
686 Q10DO activity in the EXP75. Therefore, we suggest that strong eastward GWD in the  
687 mid-to-upper mesosphere in summer need to be alleviated, which can generate more  
688 instability in the SH high-latitude mesosphere region that can lead to discrepancy from  
689 observations.

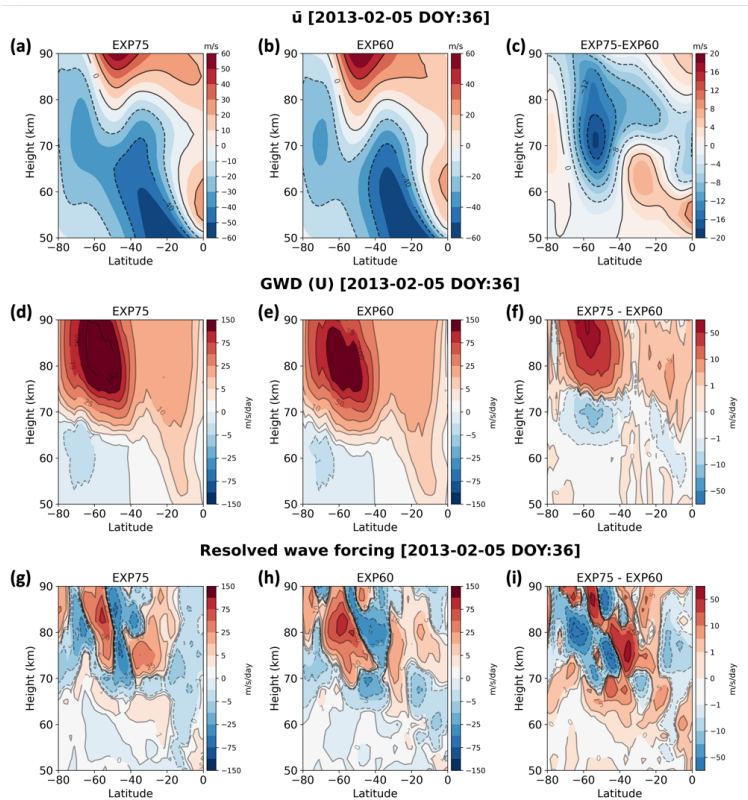
**Deleted:** also

**Deleted:** , but

**Deleted:** compensation between

**Deleted:** is

**Deleted:** valid with slight shift



695

696 **Figure 8.** Latitude-height distributions of (a–c) zonal-mean zonal wind, (d–f) zonal  
 697 component of GWD and (g–i) resolved wave forcing (EP flux divergence) in 5 February  
 698 2013 for (left) the EXP75, (middle) the EXP60, and (right) difference between EXP75  
 699 and EXP60 (EXP75–EXP60).

700

701 **4. Summary**

702 In this paper, the seasonal variation and the amplification mechanism of  
703 Q10DW during 2012–2016 in the SH high-latitude regions are investigated using two  
704 MRs located in Antarctica, and SD-WACCM simulations. Using the phase difference of  
705 meridional winds measured by two MRs, we extract westward-propagating Q10DW  
706 with zonal wavenumber 1. The seasonal variation of the observed Q10DW shows that  
707 the amplitude is strong during equinoxes, which is consistent with previous studies. In  
708 order to elucidate the amplification mechanism of Q10DW observed by MRs during  
709 equinoxes, two SD-WACCM experiments are carried out using the MERRA-2  
710 reanalysis data from surface to ~60 km (EXP60) and ~75 km (EXP75), respectively.  
711 The temporal variation of the averaged amplitude of Q10DW in the EXP75 during  
712 2012–2016 is in better agreement with the MR observations. Meanwhile, the amplitude  
713 of Q10DW in the EXP60 is excessively large, compared with the observations. Based on  
714 the analysis of meridional gradient of the QGPV and wave-activity density, the Q10DW  
715 observed in the SH high-latitude region by the MRs originated in situ around the high-  
716 latitude stratosphere-mesosphere region, where the large-scale instability or  
717 overreflection near the critical lines occur. The unrealistically large magnitude of  
718 Q10DO (quasi-10-day-like oscillations without satisfying the hemispheric symmetry  
719 unlike Q10DW) is simulated in the EXP60 during February and November. In order to  
720 understand mechanisms of the large amplitude of Q10DO in the EXP60 during the SH  
721 summer, we compare the meridional gradient of QGPV from EXP75 and EXP60. The  
722 results show that specified dynamics with MERRA-2 reanalysis data mitigate the  
723 meridional and vertical variation of zonal winds in the polar mid-to-upper mesosphere

Deleted: ¶  
Formatted: Font: (Default) +Body (Times New Roman)

Deleted: ¶

Deleted: ¶

Deleted: ¶  
Formatted: Font: (Default) +Body (Times New Roman)

Deleted: ¶

Deleted: reveal  
Formatted: Font: (Default) +Body (Times New Roman)

Deleted: ¶

731 in the EXP75, leading reduction in the large-scale instability. On the other hand, the  
732 large amplitude of Q10DO in the EXP60 is attributed to the large-scale instability  
733 related to the GWD and partially to the EPFD in the polar mid-to-upper mesosphere.  
734 The polar mesospheric GWD can lead to strong large-scale instability in the SH high-  
735 latitude mesosphere and unrealistically large amplitude of Q10DO in summer. The  
736 present study on the amplification mechanism of Q10DW during equinoxes, and the  
737 unrealistic Q10DO amplitude in summer provide potential importance of large-scale  
738 instability, which can be to a substantial degree caused by parameterized GWD, during  
739 summer in the polar mesosphere for numerical models. In this paper, we focus on the  
740 Q10DW relating to the large-scale instability and polar mesospheric GWD, but other  
741 normal modes of PW will be considered for future studies.

#### 742 **Code and Data availability**

743 The source code of Community Earth System Model 2 (CESM2) developed at  
744 the National Center for Atmospheric Research (NCAR) is available at  
745 <https://www.cesm.ucar.edu/models/cesm2>. The atmospheric forcing data for specified  
746 dynamics are available from NCAR Research Data Archive (RDA) at  
747 <https://rda.ucar.edu>.

748 The Davis station meteor radar data are available from the Australian Antarctic  
749 Data Centre at [https://data.aad.gov.au/metadata/records/Davis\\_33MHz\\_Meteor\\_Radar](https://data.aad.gov.au/metadata/records/Davis_33MHz_Meteor_Radar).  
750 The King Sejong Station meteor radar data are available from Korea Polar Data Center  
751 (KPDC) at <https://kpdc.kopri.re.kr>. The GPH data from the MLS onboard the NASA's  
752 EOS Aura satellite are available from Goddard Earth Science Data and Information  
753 Services Center (GES DISC) at <https://daac.gsfc.nasa.gov>.

Deleted: a

Deleted: ¶

756 **Author contributions**

757 WL and ISS designed the study, together with YHK, and wrote the manuscript.  
758 WL performed the analysis of the observational (MR and satellite) data in collaboration  
759 with ISS. ISS designed the SD-WACCM experiments. WL and ISS carried out the SD-  
760 WACCM experiments, ISS and BGS aided in interpreting the analysis of action  
761 conservation equation for Rossby waves. All authors discussed the results and  
762 contributed to the final manuscript.

**Deleted:** ISS, and YHK designed the study. WL and ISS carried out the SD-WACCM experiments and analysis the observational data. WL wrote the manuscript.

**Deleted:** results

**Deleted:** and worked on the manuscript

763 **Competing interests**

764 The authors declare that they have no conflict of interest.

765 **Acknowledgements**

766 This research was supported by the Korea Astronomy and Space Science  
767 Institute under the R&D program (Project No. 2023-1-850-07) supervised by the  
768 Ministry of Science and ICT.

769

770 **References**

771 Andrews, D. G., Holton, J. R., and Leovy, C. B.: Middle Atmosphere Dynamics,  
772 Elsevier, New York, USA, 489 pp., 1987.

773 Beres, J. H., Garcia, R. R., Boville, B. A., and Sassi, F.: Implementation of a gravity  
774 wave source spectrum parameterization dependent on the properties of convection in the

780 Whole Atmosphere Community Climate Model (WACCM), J. Geophys. Res.-Atmos.,  
781 110, <https://doi.org/10.1029/2004jd005504>, 2005.

782 Brakebusch, M., Randall, C. E., Kinnison, D. E., Tilmes, S., Santee, M. L., and  
783 Manney, G. L.: Evaluation of Whole Atmosphere Community Climate Model  
784 simulations of ozone during Arctic winter 2004–2005, J. Geophys. Res.-Atmos., 118,  
785 2673–2688, <https://doi.org/10.1002/jgrd.50226>, 2013.

786 [Chandran, A., Garcia, R. R., Collins, R. L., and Chang, L. C.: Secondary planetary  
787 waves in the middle and upper atmosphere following the stratospheric sudden warming  
788 event of January 2012, Geophys. Res. Lett., 40, 1861–1867,  
789 <https://doi.org/10.1002/grl.50373>, 2013.](#)

790 Charron, M. and Manzini, E.: Gravity ~~waves~~ from ~~fronts~~: Parameterization and ~~middle~~  
791 ~~atmosphere response~~ in a ~~general circulation model~~, J. Atmos. Sci., 59, 923–941,  
792 [https://doi.org/10.1175/1520-0469\(2002\)059<0923:gwffpa>2.0.co;2](https://doi.org/10.1175/1520-0469(2002)059<0923:gwffpa>2.0.co;2), 2002.

793 Cohen, N. Y., [Gerber, E. P.](#) and Bühler, ~~O.~~: Compensation between ~~resolved~~ and  
794 ~~unresolved wave driving~~ in the ~~stratosphere~~: Implications for ~~downward control~~, J.  
795 Atmos. Sci., 70, 3780–3798, <https://doi.org/10.1175/jas-d-12-0346.1>, 2013.

796 Danabasoglu, G., Lamarque, J. -F., Bacmeister, J., Bailey, D. A., DuVivier, A. K.,  
797 Edwards, J., Emmons, L. K., Fasullo, J., Garcia, R., Gettelman, A., Hannay, C.,  
798 Holland, M. M., Large, W. G., Lauritzen, P. H., Lawrence, D. M., Lenaerts, J. T. M.,  
799 Lindsay, K., Lipscomb, W. H., Mills, M. J., Neale, R., Oleson, K. W., Otto-Bliesner, B.,  
800 Phillips, A. S., Sacks, W., Tilmes, S., Kampenhout, L., Versteinsten, M., Bertini, A.,

- ~~Deleted: Waves~~
- ~~Deleted: Fronts~~
- ~~Deleted: Middle~~
- ~~Deleted: Atmosphere~~
- ~~Deleted: Response~~
- ~~Deleted: General~~
- ~~Deleted: Circulation~~
- ~~Deleted: Model~~
- ~~Deleted: E. P. G. and~~
- ~~Deleted: Resolved~~
- ~~Deleted: Unresolved~~
- ~~Deleted: Wave~~
- ~~Deleted: Driving~~
- ~~Deleted: Stratosphere~~
- ~~Deleted: Downward~~
- ~~Deleted: Control~~

817 Dennis, J., Deser, C., Fischer, C., Fox-Kemper, B., Kay, J. E., Kinnison, D., Kushner, P.  
818 J., Larson, V. E., Long, M. C., Mickelson, S., Moore, J. K., Nienhouse, E., Polvani, L.,  
819 Rasch, P. J., and Strand, W. G.: The Community Earth System Model Version 2  
820 (CESM2), *J. Adv. Model. Earth. Sy.*, 12, <https://doi.org/10.1029/2019ms001916>, 2020.

821 Day, K. A. and Mitchell, N. J.: The 5-day wave in the Arctic and Antarctic mesosphere  
822 and lower thermosphere, *J. Geophys. Res.-Atmos.*, 1984–2012, 115,  
823 <https://doi.org/10.1029/2009jd012545>, 2010.

824 Edmon, H. J., Hoskins, B. J., and McIntyre, M. E.: Eliassen-Palm cross sections for the  
825 troposphere, *J. Atmos. Sci.*, 37, 2600–2616, [https://doi.org/10.1175/1520-0469\(1980\)037<2600:epcsft>2.0.co;2](https://doi.org/10.1175/1520-0469(1980)037<2600:epcsft>2.0.co;2), 1980.

827 Egito, F., Takahashi, H., and Miyoshi, Y.: Effects of the planetary waves on the MLT  
828 airglow, *Ann. Geophys.*, 35, 1023–1032, <https://doi.org/10.5194/angeo-35-1023-2017>,  
829 2017.

830 Eswaraiah, S., Kim, Y. H., Hong, J., Kim, J.-H., Ratnam, M. V., Chandran, A., Rao, S.  
831 V. B., and Riggan, D.: Mesospheric signatures observed during 2010 minor  
832 stratospheric warming at King Sejong Station (62°S, 59°W), *J. Atmos. Sol-Terr. Phy.*,  
833 140, 55–64, <https://doi.org/10.1016/j.jastp.2016.02.007>, 2016.

834 Eswaraiah, S., Ratnam, M. V., Kim, Y. H., Kumar, K. N., Chalapathi, G. V.,  
835 Ramanajaneyulu, L., Lee, J., Prasanth, P. V., Thyagarajan, K., and Rao, S. V. B.:  
836 Advanced meteor radar observations of mesospheric dynamics during 2017 minor SSW

Deleted: Cross

Deleted: Sections

Deleted: Troposphere



840 over the tropical region, *Adv. Space. Res.*, 64, 1940–1947,  
841 <https://doi.org/10.1016/j.asr.2019.05.039>, 2019.

842 Eyring, Veronika, et al.: Overview of IGAC/SPARC Chemistry-Climate Model  
843 Initiative (CCMI) community simulations in support of upcoming ozone and climate  
844 assessments, *SPARC newsletter*, 40, 48–66, <https://oceanrep.geomar.de/id/eprint/20227>,  
845 2013.

846 Forbes, J. M. and Zhang, X.: Quasi-10-day wave in the atmosphere, *J. Geophys. Res.-*  
847 *Atmos.*, 120, 11,079–11,089, <https://doi.org/10.1002/2015jd023327>, 2015.

848 Forbes, J. M. and Zhang, X.: The quasi-6 day wave and its interactions with solar tides,  
849 *J. Geophys. Res.-Space*, 122, 4764–4776, <https://doi.org/10.1002/2017ja023954>, 2017.

850 Forbes, J. M., Hagan, M. E., Miyahara, S., Vial, F., Manson, A. H., Meek, C. E., and  
851 Portnyagin, Y. I.: Quasi 16-day oscillation in the mesosphere and lower thermosphere,  
852 *J. Geophys. Res.-Atmos.*, 100, 9149–9163, <https://doi.org/10.1029/94jd02157>, 1995.

853 Forbes, J. M., Zhang, X., Heelis, R., Stoneback, R., Englert, C. R., Harlander, J. M.,  
854 Harding, B. J., Marr, K. D., Makela, J. J., and Immel, T. J.: Atmosphere-Ionosphere (A-  
855 I) ~~coupling~~ as ~~viewed~~ by ICON: Day-to-~~day variability due to planetary wave (PW)-~~~~tide~~  
856 ~~interactions~~, *J. Geophys. Res.-Space*, 126, <https://doi.org/10.1029/2020ja028927>, 2021.

857 [Fujiwara, M., Wright, J. S., Manney, G. L., Gray, L. J., Anstey, J., Birner, T., Davis, S.,](#)  
858 [Gerber, E. P., Harvey, V. L., Hegglin, M. I., Homeyer, C. R., Knox, J. A., Krüger, K.,](#)  
859 [Lambert, A., Long, C. S., Martineau, P., Molod, A., Monge-Sanz, B. M., Santee, M. L.,](#)  
860 [Tegtmeier, S., Chabrillat, S., Tan, D. G. H., Jackson, D. R., Polavarapu, S., Compo, G.](#)

- Deleted:** Coupling
- Deleted:** Viewed
- Deleted:** Day
- Deleted:** Variability
- Deleted:** Due
- Deleted:** Planetary
- Deleted:** Wave
- Deleted:** Tide
- Deleted:** Interactions

870 [P., Dragani, R., Ebisuzaki, W., Harada, Y., Kobayashi, C., McCarty, W., Onogi, K.,](#)  
871 [Pawson, S., Simmons, A., Wargan, K., Whitaker, J. S., and Zou, C.-Z.:](#) Introduction to  
872 [the SPARC Reanalysis Intercomparison Project \(S-RIP\) and overview of the reanalysis](#)  
873 [systems, Atmos. Chem. Phys., 17, 1417–1452, \[https://doi.org/10.5194/acp-17-1417-\]\(https://doi.org/10.5194/acp-17-1417-2017\)](#)  
874 [2017, 2017.](#)

875 Gan, Q., Oberheide, J., and Pedatella, N. M.: Sources, ~~sinks~~, and ~~propagation~~  
876 ~~characteristics~~ of the ~~quasi 6-day wave~~ and ~~its impact~~ on the ~~residual mean circulation~~,  
877 J. Geophys. Res.-Atmos., 123, 9152–9170, <https://doi.org/10.1029/2018jd028553>, 2018.

878 Gelaro, R., McCarty, W., Suárez, M. J., Todling, R., Molod, A., Takacs, L., Randles, C.  
879 A., Darmenov, A., Bosilovich, M. G., Reichle, R., Wargan, K., Coy, L., Cullather, R.,  
880 Draper, C., Akella, S., Buchard, V., Conaty, A., Silva, A. M. da, Gu, W., Kim, G.-K.,  
881 Koster, R., Lucchesi, R., Merkova, D., Nielsen, J. E., Partyka, G., Pawson, S., Putman,  
882 W., Rienecker, M., Schubert, S. D., Sienkiewicz, M., and Zhao, B.: The Modern-Era  
883 Retrospective Analysis for Research and Applications, Version 2 (MERRA-2), J.  
884 Climate, 30, 5419–5454, <https://doi.org/10.1175/jcli-d-16-0758.1>, 2017.

885 Goncharenko, L. P., Harvey, V. L., Greer, K. R., Zhang, S. -R., and Coster, A. J.:  
886 Longitudinally ~~dependent low-latitude ionospheric disturbances linked~~ to the Antarctic  
887 ~~sudden stratospheric warming~~ of September 2019, J. Geophys. Res.-Space, 125,  
888 <https://doi.org/10.1029/2020ja028199>, 2020.

889 [Harvey, V. L., Knox, J. A., France, J. A., Fujiwara, M., Gray, L., Hirooka, T.,](#)  
890 [Hitchcock, P., Hitchman, M., Kawatani, Y., Manney, G. L., McCormack, J., Orsolini,](#)  
891 [Y., Sakazaki, T., and Tomikawa, Y.:](#) Chapter 11: Upper Stratosphere and Lower

**Deleted:** Sinks

**Deleted:** Propagation

**Deleted:** Characteristics

**Deleted:** Quasi

**Deleted:** Day

**Deleted:** Wave

**Deleted:** Its

**Deleted:** Impact

**Deleted:** Residual

**Deleted:** Mean

**Deleted:** Circulation

**Deleted:** Dependent

**Deleted:** Low

**Deleted:** Latitude

**Deleted:** Ionospheric

**Deleted:** Disturbances

**Deleted:** Linked

**Deleted:** Sudden

**Deleted:** Stratospheric

**Deleted:** Warming

912 [Mesosphere, SPARC Reanalysis Intercomparison Project \(S-RIP\) Final Report](#), edited  
 913 [by: Fujiwara, M., Manney, G. L., Gray, L. J., and Wright, J. S., SPARC Report No. 10,](#)  
 914 [WCRP-6/2021, SPARC, DLR-IPA, Oberpfaffenhofen, Germany,](#)  
 915 <https://doi.org/10.17874/800dee57d13>, 2021.

916 Harvey, V. L., Randall, C. E., Becker, E., Smith, A. K., Bardeen, C. G., France, J. A.,  
 917 and Goncharenko, L. P.: Evaluation of the [mesospheric polar vortices](#) in WACCM, J.  
 918 Geophys. Res.-Atmos., 124, 10626–10645, <https://doi.org/10.1029/2019jd030727>,  
 919 2019.

920 [He, M., Chau, J. L., Stober, G., Li, G., Ning, B., and Hoffmann, P.: Relations between](#)  
 921 [semidiurnal tidal variants through diagnosing the zonal wavenumber using a phase](#)  
 922 [differencing technique based on two ground-based detectors](#), J. Geophys. Res.-Atmos.,  
 923 123, 4015–4026, <https://doi.org/10.1002/2018jd028400>, 2018.

924 [He, M., Chau, J. L., Forbes, J. M., Thorsen, D., Li, G., Siddiqui, T. A., Yamazaki, Y.,](#)  
 925 [and Hocking, W. K.: Quasi-10-day wave and semidiurnal tide nonlinear interactions](#)  
 926 [during the Southern Hemispheric SSW 2019 observed in the Northern Hemispheric](#)  
 927 [mesosphere](#), Geophys. Res. Lett., 47, <https://doi.org/10.1029/2020gl091453>, 2020a.

928 [He, M., Yamazaki, Y., Hoffmann, P., Hall, C. M., Tsutsumi, M., Li, G., and Chau, J. L.:](#)  
 929 [Zonal wave number diagnosis of Rossby wave-like oscillations using paired ground-](#)  
 930 [based radars](#), J. Geophys. Res.-Atmos., 125, <https://doi.org/10.1029/2019jd031599>,  
 931 2020b.

- Deleted: Mesospheric
- Deleted: Polar
- Deleted: Vortices
- Moved (insertion) [1]
- Deleted: B
- Deleted: S
- Deleted: T
- Deleted: V
- Deleted: T
- Deleted: D
- Deleted: Z
- Deleted: W
- Deleted: U
- Deleted: P
- Deleted: D
- Deleted: T
- Deleted: B
- Deleted: T
- Deleted: G
- Deleted: B
- Deleted: D
- Field Code Changed
- Deleted: ¶
- Deleted: D
- Deleted: W
- Deleted: S
- Deleted: T
- Deleted: N
- Deleted: I
- Deleted: D
- Deleted: O
- Deleted: M
- Moved up [1]: He, M., Chau, J. L., Stober, G., Li, G., Ning, B., and Hoffmann, P.: Relations Between Semidiurnal Tidal Variants
- Deleted: Wave
- Deleted: Number
- Deleted: Diagnosis
- Deleted: Wave
- Deleted: Like
- Deleted: Oscillations
- Deleted: Using
- Deleted: Paired
- Deleted: Ground
- Deleted: Based
- Deleted: Radars

982 Hirooka, T.: Normal ~~mode~~ Rossby ~~waves~~ as ~~revealed~~ by UARS/ISAMS ~~observations~~, J.  
983 Atmos. Sci., 57, 1277–1285, <https://doi.org/10.1175/1520->  
984 0469(2000)057<1277:NMRWAR>2.0.CO;2, 2000.

~~Deleted: Mode~~  
~~Deleted: Waves~~  
~~Deleted: Revealed~~  
~~Deleted: Observations~~

985 Holdsworth, D. A., Murphy, D. J., Reid, I. M., and Morris, R. J.: Antarctic meteor  
986 observations using the Davis MST and meteor radars, Adv. Space Res., 42, 143–154,  
987 <https://doi.org/10.1016/j.asr.2007.02.037>, 2008.

988 Huang, C., Zhang, S., Chen, G., Zhang, S., and Huang, K.: Planetary ~~wave~~  
989 ~~characteristics~~ in the ~~lower atmosphere over~~ Xianghe (117.00°E, 39.77°N), China,  
990 ~~revealed~~ by the Beijing MST ~~radar~~ and MERRA ~~data~~, J. Geophys. Res.-Atmos., 122,  
991 9745–9758, <https://doi.org/10.1002/2017jd027029>, 2017.

~~Deleted: Wave~~

~~Deleted: Characteristics~~  
~~Deleted: Lower~~  
~~Deleted: Atmosphere~~  
~~Deleted: Over~~  
~~Deleted: Revealed~~  
~~Deleted: Radar~~  
~~Deleted: Data~~

992 Huang, C., Li, W., Zhang, S., Chen, G., Huang, K., and Gong, Y.: Investigation of  
993 dominant traveling 10-day wave components using long-term MERRA-2 database,  
994 Earth Planets Space, 73, 85, <https://doi.org/10.1186/s40623-021-01410-7>, 2021.

995 Huang, Y.-Y., Cui, J., Li, H.-J., and Li, C.-Y.: Inter-annual variations of 6.5-day  
996 planetary waves and their relations with QBO, Earth Planet. Phys., 6, 135–148,  
997 <https://doi.org/10.26464/epp2022005>, 2022.

998 Jablonowski, C. and Williamson, D. L.: Numerical ~~techniques for global atmospheric~~  
999 ~~models~~, Lect. Notes Comput. Sci. Eng., 381–493, <https://doi.org/10.1007/978-3-642->  
1000 [11640-7\\_13](https://doi.org/10.1007/978-3-642-11640-7_13), 2011.

~~Deleted: T~~  
~~Deleted: G~~  
~~Deleted: A~~  
~~Deleted: M~~

1001 Lee, W., Song, I., Kim, J., Kim, Y. H., Jeong, S., Eswaraiah, S., and Murphy, D. J.: The  
1002 ~~observation~~ and SD-WACCM ~~simulation~~ of ~~planetary wave activity~~ in the ~~middle~~

~~Deleted: Observation~~  
~~Deleted: Simulation~~  
~~Deleted: Planetary~~  
~~Deleted: Wave~~  
~~Deleted: Activity~~  
~~Deleted: Middle~~

1025 ~~atmosphere during~~ the 2019 Southern Hemispheric ~~sudden stratospheric warming~~, J.  
1026 Geophys. Res.-Space, 126, <https://doi.org/10.1029/2020ja029094>, 2021.

1027 Lee, W., Lee, C., Kim, J., Kam, H., and Kim, Y. H.: A ~~modeling analysis~~ of the  
1028 ~~apparent linear relation between mesospheric temperatures and meteor height~~  
1029 ~~distributions measured by a meteor radar~~, J. Geophys. Res.-Space, 127,  
1030 <https://doi.org/10.1029/2021ja029812>, 2022.

1031 Lee, W., Kim, Y. H., Lee, C., and Wu, Q.: First ~~comparison of mesospheric winds~~  
1032 ~~measured~~ with a Fabry-Perot ~~interferometer~~ and ~~meteor radar~~ at the King Sejong Station  
1033 (62.2°S, 58.8°W), J. Astron. Space Sci., <https://doi.org/10.5140/JASS.2018.35.4.235>,  
1034 2018

1035 Li, W., Huang, C., and Zhang, S.: Global characteristics of the westward-propagating  
1036 quasi-16-day wave with zonal wavenumber 1 and the connection with the 2012/2013  
1037 SSW revealed by ERA-Interim, Earth Planets Space, 73, 113,  
1038 <https://doi.org/10.1186/s40623-021-01431-2>, 2021.

1039 Lindzen, R. S., Farrell, B., and Tung, K.-K.: The ~~concept of wave overreflection and its~~  
1040 ~~application to baroclinic instability~~, J. Atmos. Sci., 37, 44–63,  
1041 [https://doi.org/10.1175/1520-0469\(1980\)037<0044:tcowoa>2.0.co;2](https://doi.org/10.1175/1520-0469(1980)037<0044:tcowoa>2.0.co;2), 1980.

1042 Liu, G., Janches, D., Lieberman, R. S., Moffat-Griffin, T., Mitchell, N. J., Kim, J., and  
1043 Lee, C.: Wind ~~variations~~ in the ~~mesosphere~~ and ~~lower thermosphere near 60°S latitude~~  
1044 ~~during~~ the 2019 Antarctic ~~sudden stratospheric warming~~, J. Geophys. Res.-Space, 126,  
1045 <https://doi.org/10.1029/2020ja028909>, 2021.

**Deleted:** Atmosphere

**Deleted:** During

**Deleted:** Sudden

**Deleted:** Stratospheric

**Deleted:** Warming

**Deleted:** Modeling

**Deleted:** Analysis

**Deleted:** Apparent

**Deleted:** Linear

**Deleted:** Relation

**Deleted:** Between

**Deleted:** Mesospheric

**Deleted:** Temperatures

**Deleted:** Meteor

**Deleted:** Height

**Deleted:** Distributions

**Deleted:** Measured

**Deleted:** Meteor

**Deleted:** Radar

**Deleted:** C

**Deleted:** Mesospheric

**Deleted:** Winds

**Deleted:** Measured

**Deleted:** Interferometer

**Deleted:** Meteor

**Deleted:** Radar

**Deleted:** C

**Deleted:** Wave

**Deleted:** Overreflection

**Deleted:** Its

**Deleted:** Application

**Deleted:** Baroclinic

**Deleted:** Instability

**Deleted:** Variations

**Deleted:** Mesosphere

**Deleted:** Lower

**Deleted:** Thermosphere

**Deleted:** Near

**Deleted:** Latitude

**Deleted:** During

**Deleted:** Sudden

**Deleted:** Stratospheric

**Deleted:** Warming

1089 Liu, G., Janches, D., Ma, J., Lieberman, R. S., Stober, G., Moffat-Griffin, T., Mitchell,

1090 N. J., Kim, J., Lee, C., and Murphy, D. J.: Mesosphere and ~~lower thermosphere winds~~

1091 and ~~tidal variations during~~ the 2019 Antarctic ~~sudden stratospheric warming~~, J.

1092 Geophys. Res.-Space, 127, <https://doi.org/10.1029/2021ja030177>, 2022.

1093 Luo, J., Gong, Y., Ma, Z., Zhang, S., Zhou, Q., Huang, C., Huang, K., Yu, Y., and Li,

1094 G.: Study of the ~~quasi 10-day waves~~ in the MLT ~~region during~~ the 2018 February SSW

1095 by a ~~meteor radar chain~~, J. Geophys. Res.-Space, 126,

1096 <https://doi.org/10.1029/2020ja028367>, 2021.

1097 Ma, Z., Gong, Y., Zhang, S., Xiao, Q., Xue, J., Huang, C., and Huang, K.:

1098 Understanding the ~~excitation of quasi-6-day waves in both hemispheres during the~~

1099 September 2019 Antarctic SSW, J. Geophys. Res.-Atmos., 127,

1100 <https://doi.org/10.1029/2021jd035984>, 2022.

1101 Marsh, D. R., Mills, M. J., Kinnison, D. E., Lamarque, J.-F., Calvo, N., and Polvani, L.

1102 M.: Climate ~~change~~ from 1850 to 2005 ~~simulated~~ in CESM1(WACCM), J. Climate, 26,

1103 130509150556003, <https://doi.org/10.1175/jcli-d-12-00558.1>, 2013.

1104 Matsuno, T.: Vertical ~~propagation of stationary planetary waves in the winter~~ Northern

1105 Hemisphere, J. Atmos. Sci., 27, 871–883, [https://doi.org/10.1175/1520-](https://doi.org/10.1175/1520-0469(1970)027<0871:vpospw>2.0.co;2)

1106 [0469\(1970\)027<0871:vpospw>2.0.co;2](https://doi.org/10.1175/1520-0469(1970)027<0871:vpospw>2.0.co;2), 1970.

1107 Matthias, V. and Ern, M.: On the origin of the mesospheric quasi-stationary planetary

1108 waves in the unusual Arctic winter 2015/2016, Atmos. Chem. Phys., 18, 4803–4815,

1109 <https://doi.org/10.5194/acp-18-4803-2018>, 2018.

~~Deleted: Lower~~

~~Deleted: Thermosphere~~

~~Deleted: Winds~~

~~Deleted: Tidal~~

~~Deleted: Variations~~

~~Deleted: During~~

~~Deleted: Sudden~~

~~Deleted: Stratospheric~~

~~Deleted: Warming~~

~~Deleted: Q~~

~~Deleted: Day~~

~~Deleted: Waves~~

~~Deleted: Region~~

~~Deleted: During~~

~~Deleted: Meteor~~

~~Deleted: Radar~~

~~Deleted: Chain~~

~~Deleted: Excitation~~

~~Deleted: Quasi~~

~~Deleted: Day~~

~~Deleted: Waves~~

~~Deleted: Both~~

~~Deleted: Hemispheres~~

~~Deleted: During~~

~~Deleted: Change~~

~~Deleted: Simulated~~

~~Deleted: P~~

~~Deleted: Stationary~~

~~Deleted: Planetary~~

~~Deleted: W~~

~~Deleted: Winter~~

1141 [Matthias, V., Hoffmann, P., Rapp, M., and Baumgarten, G.: Composite analysis of the](#)  
1142 [temporal development of waves in the polar MLT region during stratospheric](#)  
1143 [warmings, J. Atmos. Sol.-Terr. Phys., 90, 86–96,](#)  
1144 <https://doi.org/10.1016/j.jastp.2012.04.004>, 2012.

1145 [McCormack, J. P., Harvey, V. L., Randall, C. E., Pedatella, N., Koshin, D., Sato, K.,](#)  
1146 [Coy, L., Watanabe, S., Sassi, F., and Holt, L. A.: Intercomparison of middle](#)  
1147 [atmospheric meteorological analyses for the Northern Hemisphere winter 2009–2010,](#)  
1148 [Atmos. Chem. Phys., 21, 17577–17605, https://doi.org/10.5194/acp-21-17577-2021,](#)  
1149 [2021.](#)

1150 McFarlane, N. A.: The ~~effect of orographically excited gravity wave drag on the general~~  
1151 ~~circulation of the lower stratosphere and troposphere~~, J. Atmos. Sci., 44, 1775–1800,  
1152 [https://doi.org/10.1175/1520-0469\(1987\)044<1775:teoeg>2.0.co;2](https://doi.org/10.1175/1520-0469(1987)044<1775:teoeg>2.0.co;2), 1987.

1153 Meyer, C. K. and Forbes, J. M.: A 6.5-day westward propagating planetary wave:  
1154 Origin and characteristics, J. Geophys. Res.-Atmos., 102, 26173–26178,  
1155 <https://doi.org/10.1029/97jd01464>, 1997.

1156 Mitra, G., Guharay, A., Batista, P. P., and Buriti, R. A.: Impact of the September 2019  
1157 ~~minor sudden stratospheric warming on the low-latitude middle atmospheric planetary~~  
1158 ~~wave dynamics~~, J. Geophys. Res.-Atmos., 127, <https://doi.org/10.1029/2021jd035538>,  
1159 2022.

**Deleted:** Effect

**Deleted:** Orographically

**Deleted:** Excited

**Deleted:** Gravity

**Deleted:** Wave

**Deleted:** Drag

**Deleted:** General

**Deleted:** Circulation

**Deleted:** Lower

**Deleted:** Stratosphere

**Deleted:** Troposphere

**Deleted:** M

**Deleted:** Sudden

**Deleted:** Stratospheric

**Deleted:** Warming

**Deleted:** Low

**Deleted:** Latitude

**Deleted:** Middle

**Deleted:** Atmospheric

**Deleted:** Planetary

**Deleted:** Wave

**Deleted:** Dynamics

1182 Palmer, T. N.: Properties of the Eliassen-Palm ~~flux~~ for ~~planetary scale motions~~, J.

1183 Atmos. Sci., 39, 992–997, [https://doi.org/10.1175/1520-](https://doi.org/10.1175/1520-0469(1982)039<0992:potepf>2.0.co;1982)

1184 [0469\(1982\)039<0992:potepf>2.0.co](https://doi.org/10.1175/1520-0469(1982)039<0992:potepf>2.0.co;1982), 1982.

1185 Qin, Y., Gu, S., Dou, X., Gong, Y., Chen, G., Zhang, S., and Wu, Q.: Climatology of

1186 the ~~quasi-6-day wave~~ in the ~~mesopause region~~ and ~~its modulations on total electron~~

1187 ~~content during~~ 2003–2017, J. Geophys. Res.-Space, 124, 573–583,

1188 <https://doi.org/10.1029/2018ja025981>, 2019.

1189 ~~Qin, Y., Gu, S., Dou, X., Teng, C., Yang, Z., and Sun, R.: Southern Hemisphere~~

1190 ~~response to the secondary planetary waves generated during the Arctic sudden~~

1191 ~~stratospheric final warmings: Influence of the quasi-biennial oscillation~~, J. Geophys.

1192 Res.-Atmos., 127, <https://doi.org/10.1029/2022jd037730>, 2022.

1193 Qin, Y., Gu, S., Teng, C., Dou, X., Yu, Y., and Li, N.: Comprehensive ~~study~~ of the

1194 ~~climatology~~ of the ~~quasi-6-day wave~~ in the ~~MLT region based~~ on Aura/MLS

1195 ~~observations~~ and SD-WACCM-X ~~simulations~~, J. Geophys. Res.-Space, 126,

1196 <https://doi.org/10.1029/2020ja028454>, 2021.

1197 Reynolds, R. W., Rayner, N. A., Smith, T. M., Stokes, D. C., and Wang, W.: An

1198 ~~improved in situ~~ and ~~satellite SST analysis~~ for ~~climate~~, J. Climate, 15, 1609–1625,

1199 [https://doi.org/10.1175/1520-0442\(2002\)015<1609:aiisas>2.0.co;2](https://doi.org/10.1175/1520-0442(2002)015<1609:aiisas>2.0.co;2), 2002.

1200 Rhodes, C. T., Limpasuvan, V., and Orsolini, Y. J.: Eastward-~~propagating planetary~~

1201 ~~waves prior~~ to the January 2009 ~~sudden stratospheric warming~~, J. Geophys. Res.-

1202 Atmos., 126, <https://doi.org/10.1029/2020jd033696>, 2021.

**Deleted:** Flux ...lux for Planetary ...lanetary Scale ...cale N... [1]

**Deleted:** Quasi...uasi-6-Day ...ay Wave ...ave in the Mesopause mesopause Region ...egion and Its ...ts Modulations ...odulations on Total ...otal Electron ...lectron Content ...ontent During ... [2]

**Deleted:** R...esponse to the S...econdary P...lanetary W...aves G...enerated D...uring the Arctic S...udden S...tratospheric F...inal W...armings: Influence of the Q...uasi-B...iennial O... [3]

**Deleted:** Study ...tudy of the Climatology ...limatology of the Quasi...uasi-6-Day ...ay Wave ...ave in the MLT Region ...egion Based ...ased on Aura/MLS Observations ...bservations and SD-WACCM-X Simulations ... [4]

**Deleted:** I...mproved In ...n Situ ...itu and Satellite ...atellite SST Analysis ...analysis for Climate ... [5]

**Deleted:** Propagating ...ropagating Planetary ...lanetary Waves waves Prior ...rior to the January 2009 Sudden ...udden Stratospheric ...tratospheric Warming ... [6]



1269 Richter, J. H., Sassi, F., and Garcia, R. R.: Toward a physically based gravity wave  
1270 source parameterization in a general circulation model, J. Atmos. Sci., 67, 136–156,  
1271 <https://doi.org/10.1175/2009jas3112.1>, 2010.

1272 Salby, M. L.: Rossby normal modes in nonuniform background configurations. Part I:  
1273 Simple fields, J. Atmos. Sci., 38, 1803–1826, [https://doi.org/10.1175/1520-](https://doi.org/10.1175/1520-0469(1981)038<1803:rnminb>2.0.co;2)  
1274 [0469\(1981\)038<1803:rnminb>2.0.co;2](https://doi.org/10.1175/1520-0469(1981)038<1803:rnminb>2.0.co;2), 1981a.

1275 Salby, M. L.: Rossby normal modes in nonuniform background configurations. Part II.  
1276 Equinox and solstice conditions, J. Atmos. Sci., 38, 1827–1840,  
1277 [https://doi.org/10.1175/1520-0469\(1981\)038<1827:rnminb>2.0.co;2](https://doi.org/10.1175/1520-0469(1981)038<1827:rnminb>2.0.co;2), 1981b.

1278 Salby, M. L.: Survey of planetary-scale traveling waves: The state of theory and  
1279 observations, Rev. Geophys., 22, 209–236, <https://doi.org/10.1029/rg022i002p00209>,  
1280 1984.

1281 Sassi, F., McCormack, J. P., Tate, J. L., Kuhl, D. D., and Baker, N. L.: Assessing the  
1282 impact of middle atmosphere observations on day-to-day variability in lower  
1283 thermospheric winds using WACCM-X, J. Atmos. Sol.-Terr. Phys., 212, 105486,  
1284 <https://doi.org/10.1016/j.jastp.2020.105486>, 2021.

1285 Sassi, F. and Liu, H.-L.: Westward traveling planetary wave events in the lower  
1286 thermosphere during solar minimum conditions simulated by SD-WACCM-X, J.  
1287 Atmos. Sol.-Terr. Phys., 119, 11–26, https://doi.org/10.1016/j.jastp.2014.06.009, 2014.

1288 Sato, K., Yasui, R., and Miyoshi, Y.: The momentum budget in the stratosphere,  
1289 mesosphere, and lower thermosphere. Part I: Contributions of different wave types and

- Deleted:** Physically
- Deleted:** Based
- Deleted:** Gravity
- Deleted:** Wave
- Deleted:** Source
- Deleted:** Parameterization
- Deleted:** General
- Deleted:** Circulation
- Deleted:** Model
- Deleted:** Normal
- Deleted:** Modes
- Deleted:** Nonuniform
- Deleted:** Background
- Deleted:** Configurations
- Deleted:** Fields
- Deleted:** Normal
- Deleted:** Modes
- Deleted:** Nonuniform
- Deleted:** Background
- Deleted:** Configurations
- Deleted:** Solstice
- Deleted:** Conditions
- Deleted:** Momentum
- Deleted:** Budget
- Deleted:** Stratosphere
- Deleted:** Mesosphere
- Deleted:** Lower
- Deleted:** Thermosphere
- Deleted:** Different
- Deleted:** Wave
- Deleted:** Types

1321 in situ generation of Rossby waves, J. Atmos. Sci., 75, 3613–3633,

1322 <https://doi.org/10.1175/jas-d-17-0336.1>, 2018.

1323 Schwartz, M. J., Lambert, A., Manney, G. L., Read, W. G., Livesey, N. J., Froidevaux,  
1324 L., Ao, C. O., Bernath, P. F., Boone, C. D., Cofield, R. E., Daffer, W. H., Drouin, B. J.,  
1325 Fetzer, E. J., Fuller, R. A., Jarnot, R. F., Jiang, J. H., Jiang, Y. B., Knosp, B. W.,  
1326 Krüger, K., Li, J. -L. F., Mlynczak, M. G., Pawson, S., Russell, J. M., Santee, M. L.,  
1327 Snyder, W. V., Stek, P. C., Thurstans, R. P., Tompkins, A. M., Wagner, P. A., Walker,  
1328 K. A., Waters, J. W., and Wu, D. L.: Validation of the Aura Microwave Limb Sounder  
1329 temperature and geopotential height measurements, J. Geophys. Res.-Atmos. 1984  
1330 2012, 113, <https://doi.org/10.1029/2007jd008783>, 2008.

1331 Song, B.-G., Chun, H.-Y., and Song, I.-S.: Role of gravity waves in a vortex-split

1332 sudden stratospheric warming in January 2009, J. Atmos. Sci., 77, 3321–3342,

1333 <https://doi.org/10.1175/jas-d-20-0039.1>, 2020.

1334 Thorncroft, C. D., Hoskins, B. J., and McIntyre, M. E.: Two paradigms of baroclinic-  
1335 wave life-cycle behaviour, Q. J. Roy. Meteor. Soc., 119, 17–55,  
1336 <https://doi.org/10.1002/qj.49711950903>, 1993.

1337 Torrence, C. and Compo, G. P.: A practical guide to wavelet analysis, B. Am. Meteorol.

1338 Soc., 79, 61–78, [https://doi.org/10.1175/1520-0477\(1998\)079<0061:apgtwa>2.0.co;2](https://doi.org/10.1175/1520-0477(1998)079<0061:apgtwa>2.0.co;2),

1339 1998.

1340 Walker, S. N., Sahraoui, F., Balikhin, M. A., Belmont, G., Pinçon, J. L., Rezeau, L.,

1341 Alleyne, H., Cornilleau-Wehrin, N., and André, M.: A comparison of wave mode

Deleted: In

Deleted: Situ

Deleted: Generation

Deleted: Waves

Deleted: Gravity

Deleted: Waves

Deleted: Vortex

Deleted: Split

Deleted: Sudden

Deleted: Stratospheric

Deleted: Warming

Deleted: Practical

Deleted: Guide

Deleted: Wavelet

Deleted: Analysis

1357 identification techniques, Ann. Geophys., 22, 3021–3032,  
1358 <https://doi.org/10.5194/angeo-22-3021-2004>, 2004.

1359 Wang, J. C., Palo, S. E., Forbes, J. M., Marino, J., Moffat-Griffin, T., and Mitchell, N.

1360 J.: Unusual Quasi 10-Day Planetary ~~wave activity~~ and the ~~ionospheric response during~~  
1361 the 2019 Southern Hemisphere ~~sudden~~ Stratospheric Warming, J. Geophys. Res.-Space,  
1362 126, <https://doi.org/10.1029/2021ja029286>, 2021.

1363 Yamazaki, Y. and Matthias, V.: Large ~~amplitude quasi-10-day waves in the middle~~  
1364 ~~atmosphere during final warmings~~, J. Geophys. Res.-Atmos., 124, 9874–9892,  
1365 <https://doi.org/10.1029/2019jd030634>, 2019.

1366 Yin, S., Ma, Z., Gong, Y., Zhang, S., and Li, G.: Response of quasi-10-day waves in the  
1367 ~~MLT region to the sudden stratospheric warming in March 2020~~, Adv. Space Res., 71,  
1368 ~~298–305~~, <https://doi.org/10.1016/j.asr.2022.10.054>, 2023.

**Deleted:** Wave

**Deleted:** Activity

**Deleted:** Ionospheric

**Deleted:** Response

**Deleted:** During

**Deleted:** Sudden

**Deleted:** Amplitude

**Deleted:** Quasi

**Deleted:** Day

**Deleted:** Waves

**Deleted:** Middle

**Deleted:** Atmosphere

**Deleted:** During

**Deleted:** Final

**Deleted:** Warmings

**Page 48: [1] Deleted      In-Sun Song      1/1/24 3:35:00 PM**



**Page 48: [1] Deleted      In-Sun Song      1/1/24 3:35:00 PM**



**Page 48: [1] Deleted      In-Sun Song      1/1/24 3:35:00 PM**



**Page 48: [1] Deleted      In-Sun Song      1/1/24 3:35:00 PM**



**Page 48: [2] Deleted      In-Sun Song      1/1/24 3:36:00 PM**



**Page 48: [2] Deleted      In-Sun Song      1/1/24 3:36:00 PM**



**Page 48: [2] Deleted      In-Sun Song      1/1/24 3:36:00 PM**



**Page 48: [2] Deleted      In-Sun Song      1/1/24 3:36:00 PM**



**Page 48: [2] Deleted      In-Sun Song      1/1/24 3:36:00 PM**



**Page 48: [2] Deleted      In-Sun Song      1/1/24 3:36:00 PM**



**Page 48: [2] Deleted      In-Sun Song      1/1/24 3:36:00 PM**



**Page 48: [2] Deleted      In-Sun Song      1/1/24 3:36:00 PM**



**Page 48: [2] Deleted      In-Sun Song      1/1/24 3:36:00 PM**



**Page 48: [2] Deleted      In-Sun Song      1/1/24 3:36:00 PM**



**Page 48: [2] Deleted      In-Sun Song      1/1/24 3:36:00 PM**



**Page 48: [3] Deleted      In-Sun Song      1/1/24 3:36:00 PM**



**Page 48: [3] Deleted      In-Sun Song      1/1/24 3:36:00 PM**



**Page 48: [3] Deleted      In-Sun Song      1/1/24 3:36:00 PM**



**Page 48: [3] Deleted      In-Sun Song      1/1/24 3:36:00 PM**



**Page 48: [3] Deleted      In-Sun Song      1/1/24 3:36:00 PM**



**Page 48: [3] Deleted      In-Sun Song      1/1/24 3:36:00 PM**



**Page 48: [3] Deleted      In-Sun Song      1/1/24 3:36:00 PM**



**Page 48: [3] Deleted      In-Sun Song      1/1/24 3:36:00 PM**



**Page 48: [3] Deleted      In-Sun Song      1/1/24 3:36:00 PM**



**Page 48: [3] Deleted      In-Sun Song      1/1/24 3:36:00 PM**



**Page 48: [3] Deleted      In-Sun Song      1/1/24 3:36:00 PM**



**Page 48: [3] Deleted      In-Sun Song      1/1/24 3:36:00 PM**



**Page 48: [3] Deleted      In-Sun Song      1/1/24 3:36:00 PM**



**Page 48: [4] Deleted      In-Sun Song      1/1/24 3:37:00 PM**



**Page 48: [4] Deleted      In-Sun Song      1/1/24 3:37:00 PM**



**Page 48: [4] Deleted      In-Sun Song      1/1/24 3:37:00 PM**



**Page 48: [4] Deleted      In-Sun Song      1/1/24 3:37:00 PM**



**Page 48: [4] Deleted      In-Sun Song      1/1/24 3:37:00 PM**



**Page 48: [4] Deleted      In-Sun Song      1/1/24 3:37:00 PM**



**Page 48: [4] Deleted      In-Sun Song      1/1/24 3:37:00 PM**





**Page 48: [4] Deleted      In-Sun Song      1/1/24 3:37:00 PM**



**Page 48: [4] Deleted      In-Sun Song      1/1/24 3:37:00 PM**



**Page 48: [5] Deleted      In-Sun Song      1/1/24 3:37:00 PM**



**Page 48: [5] Deleted      In-Sun Song      1/1/24 3:37:00 PM**



**Page 48: [5] Deleted      In-Sun Song      1/1/24 3:37:00 PM**



**Page 48: [5] Deleted      In-Sun Song      1/1/24 3:37:00 PM**



**Page 48: [5] Deleted      In-Sun Song      1/1/24 3:37:00 PM**



**Page 48: [5] Deleted      In-Sun Song      1/1/24 3:37:00 PM**



**Page 48: [6] Deleted      In-Sun Song      1/1/24 3:37:00 PM**



**Page 48: [6] Deleted      In-Sun Song      1/1/24 3:37:00 PM**



**Page 48: [6] Deleted      In-Sun Song      1/1/24 3:37:00 PM**



**Page 48: [6] Deleted      In-Sun Song      1/1/24 3:37:00 PM**



**Page 48: [6] Deleted      In-Sun Song      1/1/24 3:37:00 PM**



**Page 48: [6] Deleted      In-Sun Song      1/1/24 3:37:00 PM**



▼.....

▲.....